



BIROn - Birkbeck Institutional Research Online

Smith, Adam G.G. and Fox, M. and Schwanghart, W. and Carter, Andrew (2022) Comparing methods for calculating channel steepness index. *Earth-Science Reviews* 227 (103970), ISSN 0012-8252.

Downloaded from: <https://eprints.bbk.ac.uk/id/eprint/47537/>

Usage Guidelines:

Please refer to usage guidelines at <https://eprints.bbk.ac.uk/policies.html> or alternatively contact lib-eprints@bbk.ac.uk.

Comparing methods for calculating channel steepness index

Adam G G Smith^{a,b,*}, Matthew Fox^b, Wolfgang Schwanghart^c, Andrew Carter^{a,b}

^a*Department of Earth & Planetary Science Birkbeck, University of London, Malet St., London WC1E 7HX, UK*

^b*London Geochronology Centre, University College London, University of London, London WC1E 6BT, UK*

^c*Institute of Environmental Science and Geography, University of Potsdam, 14476, Potsdam-Golm, Germany.*

Abstract

Channel steepness index, k_s , is a metric derived from the stream power model that, under certain conditions, scales with relative rock uplift rate. Channel steepness index is a property of rivers, which can be relatively easily extracted from digital elevation models (DEMs). As DEM data sets are widely available for Earth and are becoming more readily available for other planetary bodies, channel steepness index represents a powerful tool for interpreting tectonic processes. However, multiple approaches to calculate channel steepness index exist. From this several important questions arise; does choice of approach change the values of channel steepness index, can values be so different that choice of approach can influence the findings of a study, and are certain approaches better than others? With the aid of a synthetic river profile and a case study from the Sierra Nevada, California, we show that values of channel steepness index vary over orders of magnitude according to the methodology used in the calculation. We explore the limitations, advantages and disadvantages of the key approaches to calculating channel steepness index, and find that choosing an appropriate approach relies on the context of a study. Given these observations, it is important that authors acknowledge the methodology used to calculate channel

*Corresponding author

Email address: `adam.smith.20@ucl.ac.uk` (Adam G G Smith)

steepness index, to ensure that results can be contextualised and reproduced.

Keywords: Channel Steepness Index, Fluvial Geomorphology, Rivers, Tectonics, Geomorphology, Digital Elevation Models, Sierra Nevada

1. Introduction

Advances in creating, processing and disseminating digital elevation models (DEMs), especially global data sets (e.g., SRTM, ASTER, ALOS), have made it relatively easy to extract quantitative information from the Earth's surface, significantly increasing our understanding of how tectonic and geomorphic processes shape landscapes (Wobus et al., 2006; Tucker, 2009; Kirby & Whipple, 2012; Seybold et al., 2021). In particular, longitudinal river profiles have received much attention, as they encode information about present and past changes to tectonic and climatic regimes. One of the key metrics that characterize longitudinal river profiles is the channel steepness index, k_s , which provides a quantitative measure of relative uplift rate. As such, channel steepness index has been used to explore and infer spatial variations in rock uplift and erosion (Kirby & Whipple, 2001, 2012; Safran et al., 2005; Whittaker et al., 2008; DiBiase et al., 2010; Bernard et al., 2019), to investigate climatic and lithological influence on such variation (Cyr et al., 2014; Adams et al., 2020; Bernard et al., 2021; Harries et al., 2021), discern rock and surface uplift rate histories on a variety of spatio-temporal scales (Roberts & White, 2010; Roberts et al., 2012; Goren et al., 2014; Clubb et al., 2020), and assess drainage divide migration and reorganisation (Chen & Willett, 2016; Duvall et al., 2020). Given the importance of these processes for many hillslope and fluvial processes, k_s has also been shown to be an important predictor for geomorphological hazards and risks in high-mountain areas (Devrani et al., 2015; Schwanghart et al., 2018).

Several methods exist to calculate channel steepness and new methods continue to be developed (Hack, 1957; Flint, 1974; Whipple & Tucker, 1999; Perron & Royden, 2013; Mudd et al., 2014; Gailleton et al., 2019). These different methods have individual strengths and weaknesses, and result in variable val-

ues of k_s when applied to the same data. Choosing a particular method thus requires information on its suitability, precision and accuracy, which vary with the quality of the DEM and the context of the study. As a result, researchers
30 must carefully consider the choice of methodology for each individual study. Our aim is to review the approaches of the two main classes of methods used to calculate channel steepness index. We use a synthetic data set to highlight the advantages, disadvantages, accuracy and bias of each approach, before testing their limitations and strengths using a real world data set from the Sierra
35 Nevada, California.

1.1. *Introducing Channel Steepness*

Channel steepness index stems from the pioneering work of G.K. Gilbert. Gilbert (1877) qualitatively reasoned that a stream’s erosive power is related to ‘declivity’ or slope, which influences the flow velocity, and the volume of water in the channel. The work of Hack (1957) then quantified some of these observations, expressing the slope of a channel at any point as a power function of the channel’s upstream length. From this, Flint (1974) derived the more familiar equation,

$$S = k_s A^{-\theta} \tag{1}$$

where S is the slope, A is the upstream area, k_s is the channel steepness index and θ is the concavity index. Equation 1 provides an expression that can be used to calculate channel steepness index given the slope and upstream area for a specific point in a channel, however it is unclear what k_s represents in terms of uplift and erosion. For this, it is necessary to visit the stream power incision model (Howard & Kerby, 1983; Howard et al., 1994; Whipple & Tucker, 1999) which states that the erosion rate, E , of a river at any point is proportional to the upstream area, A , and slope, S , raised by the positive exponents m and n respectively. An erodibility constant, K , is introduced to represent the combined local impacts of climate, lithology, hydraulic and bedload parameters on the process of erosion, resulting in the following equation,

$$E = KA^m S^n. \tag{2}$$

The elevation of any point along the stream network can be considered to be the result of rock uplift and erosion. Therefore, any change with elevation through time, $\frac{dz}{dt}$, can be expressed as rock uplift rate minus erosion rate. If the rock uplift rate is greater than erosion rate, surface uplift will occur (England & Molnar, 1990). Combining an expression for rock uplift rate, u , with equation 2, we are left with the following equation to describe the change in elevation at any point on a stream network,

$$\frac{dz}{dt} = u - KA^m S^n. \quad (3)$$

If an area is in steady state, i.e. $u = E$ and $\frac{dz}{dt} = 0$, we can write,

$$u = KA^m S^n. \quad (4)$$

Slope and area can be measured using a DEM, but inferring K is problematic unless lithological, uplift rates or other geochronological evidence is available (Ferrier et al., 2013; Schwanghart & Scherler, 2020; Quye-Sawyer et al., 2020). As K combines factors of erodibility, erosivity and river geometry, it often cannot be directly measured in the field. Any determination is complicated by a lack of understanding of how different environmental and geological factors interact to influence erosion. To calculate channel steepness index from equation 4, we can first divide both sides by K , and then solve for slope to remove the exponent n from the right hand side of the equation. This creates the following expression for channel steepness index,

$$k_s = \left(\frac{u}{K}\right)^{\frac{1}{n}} = A^{\frac{m}{n}} S. \quad (5)$$

Channel steepness index is therefore equivalent to $\left(\frac{u}{K}\right)^{\frac{1}{n}}$, which can be calculated using the upstream drainage area A , to the power of m/n , or θ (expected to fall
 40 between a narrow range of values (Willgoose et al., 1990; Snyder et al., 2000; Kirby & Whipple, 2012; Croissant & Braun, 2014)), and the slope.

However, there are uncertainties associated with calculating area and slope, related to the natural variability in river gradient (e.g., through step-pool or riffle-pool sequences), DEM resolution, and the presence of artefacts and errors

45 in DEMs (Section 1.2, Fisher & Tate, 2006). Methods to calculate channel steepness differ in how they treat these uncertainties and can be broadly split into two categories; those based on equations 1 - 5 using slope and area, and those based on a variable transformation of the distance coordinate, which allows channel steepness to be calculated directly from elevation as opposed to slope.

50 1.2. Challenges of working with DEMs

A DEM is a representation of topography, created by tessellating a surface and assigning elevation values to each discrete area. Commonly, DEMs are stored as rectangular grids because the uniformity makes computations simpler and numerically more accurate. To extract river networks from rectangular
55 grids, one commonly assumes that water flows downhill along the steepest gradient (O’Callaghan & Mark, 1984). The single flow direction algorithm creates a non-diverging flow network which forms the basis for extracting the river network, a subgraph of the flow network. If we store each river pixel in a list of elevation values then the gradient between the i th pixel in the list and its
60 downstream neighbour $i - 1$ is calculated as $(z_i - z_{i-1})/(x_i - x_{i-1})$ where x is the horizontal along-river distance. Upstream area is extracted by counting the number of pixels that contribute to the flow of water at each point. In this way, it is straightforward to access large data sets of river characteristics, which can be used in the stream power model, and to calculate channel steepness index.

65 DEM data contains errors and noise for a number of reasons, from the acquisition of data from radar, to the discretisation of a global surface into pixels, to natural noise created by landslides and boulders that exist in river networks (Fisher & Tate, 2006; Schwanghart & Scherler, 2017). For example, an average error of 2m has been reported for DEMs derived from shuttle radar topographic
70 mission (SRTM) data of the US (Farr et al., 2007; Shortridge & Messina, 2011), but this error varies spatially and is often particularly high (up to and exceeding 100m) along valley-bottoms and water bodies (Holmes et al., 2000; Schwanghart & Scherler, 2017). These errors propagate to DEM derivatives so that estimates of river gradient are greatly affected by DEM noise. As channel steepness index

75 can be calculated from river gradient, or slope (equation 5), the accuracy of
calculated channel steepness values can be affected when using DEM-derived
data sets. As will be introduced later, there are methods that avoid working
with slope, reducing the influence of noise.

2. Extracting Channel Steepness

80 2.1. Slope-based approaches

2.1.1. Slope-Area Analysis

Prior to the widespread availability of DEMs, channel geometries had to be
measured either by laborious field work, by hand from topographic maps, or
by both (Hack, 1957; Morisawa, 1962; Flint, 1974). Similarly, calculations of
channel steepness index also had to be carried out by hand. In order to achieve
this, equation 1 can be rearranged so that it yields a straight line equation.
First, we can take the logarithm of both sides of equation 1, so that,

$$\log(S) = \log(k_s A^{-\theta}). \quad (6)$$

This can then be rearranged to,

$$\log(S) = \log(k_s) - \theta \log(A). \quad (7)$$

A data set of slope and upstream area could then be produced for different
points on a river, and plotted in log-log space (Fig. 1). Regressing a linear
model through this data provides a gradient equal the negative concavity index,
85 $-\theta$ (or $-m/n$) and the channel steepness index, as extracted from the y-intercept,
equal to $\log(k_s)$.

The scope of studies that used slope-area analysis was often limited by the
constraints of data collection. As noted by Morisawa (1962), ‘Work in quan-
titative geomorphology would progress more rapidly if measurements could be
90 taken directly from topographic maps’. In the following decades, DEMs allowed
researchers to gather large amounts of slope-area data for almost any region,
and compile tectonic information using channel steepness index.

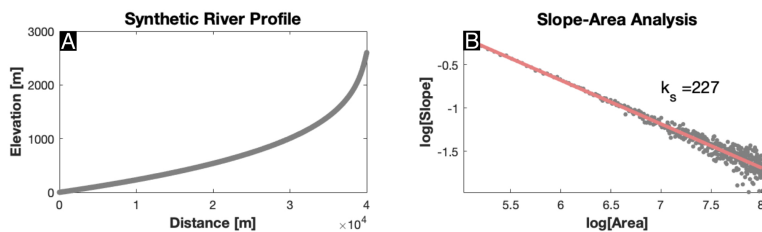


Figure 1: k_s as calculated from slope-area analysis. A. A synthetic river profile created using a k_s value of 200. Noise has been added to the synthetic profile as described in section 3.1. The noise level used is 0.5m, meaning that a random value between 0 and 0.5m has been added to each elevation point before the profile has been hydrologically conditioned. The noise level is almost imperceptible in the long profile, and is much lower than might typically be expected in DEM-derived data. B. Slope and area data extracted from the synthetic profile. Taking the logarithm of both slope and area and plotting them demonstrates how the low levels of noise in the synthetic profile are exaggerated during slope-area analysis. A line fitted through the slope-area data points has a gradient equivalent to the negative concavity index, and a y-intercept that is proportional to the k_s value.

Uncertainties in DEMs are accentuated when the derivative is taken to calculate river gradient, resulting in more scatter in slope-area plots, and ultimately
 95 in wider confidence bounds of the regression parameters k_s and m/n . There are ways in which the effects of noise on slope-area analysis can be reduced, for example, by log-bin averaging (Wobus et al., 2006). Although a binning approach can produce good results (Lague & Davy, 2003; Wobus et al., 2006), it reduces the effective resolution, and can introduce new artefacts and biases
 100 that are difficult to quantify (Perron & Royden, 2013).

2.1.2. Combating noise and pixel by pixel calculation

As will be explored later, slope-area analysis produces inaccurate results with noisy, DEM-derived data. Furthermore, as noise limits slope-area analysis, often only the strongest or largest signals within a data set can be observed using this
 105 approach. However, equation 1 expresses channel steepness index as a function of slope and area, without necessitating slope-area analysis. Using this equation, we can calculate a variant of the channel steepness index, the normalized channel steepness index, for each point on and across multiple river networks, provided

we can extract the slope and upstream area at each of these points. On a
110 discrete, hydrologically conditioned DEM, slope is $(z_i - z_{i-1})/(x_i - x_{i-1})$ and
area would be A_i and thus normalized channel steepness can be calculated at
every pixel by assuming a value for the concavity index, θ . For the purposes of
this review, we call this the pixel-by-pixel approach.

The spatial resolution of this approach is greater than slope-area analysis,
115 owing to the the shorter lengthscale over which slope and area data is aver-
aged. This aids interpretation of smaller signals. However, noise is accentuated
with this approach, some of which is unintentionally introduced by hydrological
conditioning techniques that generate stretches of zero-gradient pixels either by
filling or carving artificial sinks in the DEM (Schwanghart & Scherler, 2017).
120 To correct for this, the river profile can be smoothed prior to the extraction of
slope data (Wobus et al., 2006; Schwanghart & Scherler, 2017).

Once conditioning and smoothing have been performed, we can calculate
slope and upstream area for the extracted river profiles. However, to calculate
channel steepness index values from this data set, a reference value for the
125 concavity index, θ , must be estimated. Typical values fall between 0.4-0.6 (Kirby
& Whipple, 2012), and in certain areas, one specific value may be preferred and
widely used (Gailleton et al., 2021). For example, in the Himalaya, a reference
 θ value of approximately 0.45 was observed by Kirby & Whipple (2001), in
keeping with theoretical predictions (Whipple & Tucker, 1999) and empirical
130 observations (Snyder et al., 2000). For consistency and to allow comparison
of values, subsequent studies of the Himalayas used the same value (Wobus
et al., 2003; Hodges et al., 2004; Kirby & Whipple, 2012; Allen et al., 2013;
Scherler et al., 2014; Adams et al., 2016; Cannon et al., 2018; Adams et al.,
2020; Wahyudi et al., 2021). It is because channel steepness index is normalised
135 to a reference value of θ that it is referred to as the normalised channel steepness
index, or k_{sn} .

2.2. The integral approach

Working with slope data requires taking the derivative of the raw elevation data as extracted from a DEM. The noise inherent in these data sets is amplified by the slope calculation, which can cause the calculated values of channel steepness index to be inaccurate (Mudd et al., 2014). In order to prevent this, we can work directly with elevation data using the integral approach (Royden et al., 2000; Harkins et al., 2007; Perron & Royden, 2013).

To work with the integral approach, we take equation 1 and rewrite the slope expression as the derivative of elevation, $\frac{dz}{dx}$, so that,

$$\frac{dz}{dx} = k_s A^{-\frac{m}{n}}. \quad (8)$$

This expression can be integrated to provide an expression of channel steepness as a function of elevation. The elevation, z , at some point x , can be defined by integrating upstream from an assigned baselevel, x_b , so that,

$$z = z_b + \int_{x_b}^x \frac{k_s}{A(x')^{\frac{m}{n}}} dx'. \quad (9)$$

Equation 9 can then be modified if k_s is assumed to be spatially constant, so that,

$$z = z_b + \frac{k_s}{A_0^{\frac{m}{n}}} \int_{x_b}^x \frac{A_0^{\frac{m}{n}}}{A(x')^{\frac{m}{n}}} dx'. \quad (10)$$

The term A_0 is introduced to keep the units of the integration in metres, and the integrand is termed χ , (Royden & Perron, 2013; Perron & Royden, 2013). For a steady state river network under certain conditions (e.g. spatially invariable uplift), there is a linear relationship between elevation and χ when a suitable value of m/n is used. A plot of χ vs elevation, or a χ -plot (Fig. 2) therefore produces a straight line with a gradient proportional to channel steepness index. This straight line is used to calculate k_{sn} .

One critical advantage of working with χ is that it does not rely on the along-river gradient but instead works directly with elevation data. Calculating k_{sn} from χ -elevation data thus has far less uncertainty and error associated with it (Fig. 2).

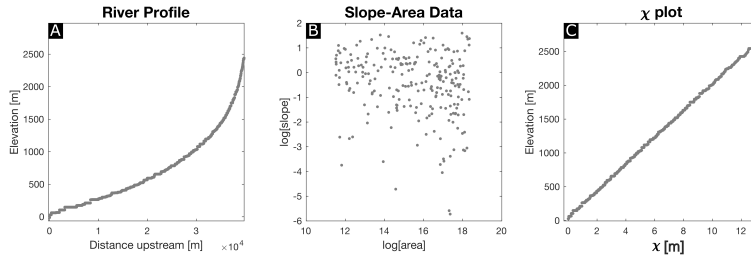


Figure 2: A - a synthetic river profile with added noise, created using a channel steepness index value of 200. B - the slope area data from the synthetic profile. C - the χ -plot for the profile. Chi-based methods are better able to deal with noisy data. It is almost impossible to fit a regression through the cloud of slope-area data, whereas it is easy to see where a line could be fitted through the χ -elevation data.

160 Another advantage of the integral approach is that the tributaries contribute to the channel steepness index estimate along a river network. The benefit of this is two-fold; working with a larger data set increases confidence in the results, and the behaviour of tributaries during the coordinate transformation can be used to constrain the concavity index (Perron & Royden, 2013; Mudd et al., 2014; Goren et al., 2014). Assuming that tributaries are in steady state and experiencing spatially uniform uplift, points in the network with similar elevations will also have similar χ values (Perron & Royden, 2013). Therefore, on a χ -plot any tributaries should be colinear with the trunk stream. This property can be exploited to determine the most likely value of m/n for a study area, with methods to do so developed by several authors (Perron & Royden, 2013; Mudd et al., 2014; Goren et al., 2014; Hergarten et al., 2016). These methods are based on calculating χ for different values of m/n , and either finding the value that minimises the misfit to the linear relationship between χ and elevation, or using a disorder metric to find the value that produces the least scatter. χ -based methods for constraining the concavity index have been shown to be superior to slope-area methods when there are transient signals propagating through the landscape or there is spatially variable uplift or erosion rates (Mudd et al., 2018). As these landscapes tend to be more interesting to study, it is no surprise that

165

170

175

χ analysis has come to the fore of tectonic geomorphology.

180 It is important to note that χ also appears in the analytical solution to the transient stream power model (Royden & Perron, 2013). In a spatially uniform area experiencing transient changes in rock uplift rate and assuming that $n = 1$, knickpoints will propagate upstream to positions on the river network that share the same χ value. In turn, a χ -elevation relationship can be interpreted as a
185 normalized rock uplift rate (Pritchard et al., 2009; Roberts et al., 2012; Royden & Perron, 2013; Goren et al., 2014). Making the assumption that erosion is spatially uniform, the approaches used to extract k_{sn} values can be used to extract uplift rates and vice versa.

2.2.1. Calculating channel steepness index using χ -elevation relationships

190 Channel steepness index can be extracted from χ -elevation data using a variety of approaches. The approaches all utilise the fact that the gradient of a χ -plot should be proportional to the channel steepness index under certain conditions. There are two categories of methods that work using this principle. The χ -elevation data can be split into unconnected segments and best fit
195 lines through the segments provide channel steepness index values. The second category works using an integration, in which the stream network is again discretised into segments, but segments are connected and constrain the calculation of other segments in the solution. The channel steepness index for each point is again taken from the gradient.

200 Within the first category of approaches, there is flexibility associated with how the χ -plot is segmented prior to calculating k_{sn} . Segments can be of equal sizes (Hilley et al., 2019) or unequal sizes (Mudd et al., 2014; Demoulin et al., 2015). Segments of equal sizes could be chosen based on either distance (Forte & Whipple, 2019), χ , or elevation (Hilley et al., 2019). If segments of differ-
205 ent sizes are used, they could be chosen by visual inspection (Demoulin et al., 2015) or selected using a segment fitting algorithm (Mudd et al., 2014). Once the segments have been selected, there is also variation in how k_{sn} values are assigned to points on the river profile. The data set could be split into non

overlapping segments, with the k_{sn} value of this segment being assigned to all
 210 points that fall within it, or the k_{sn} value of each point could be calculated so
 that the value of each point represents an average of the values either side of it
 (Gallen & Wegmann, 2017).

The choice of method for calculating channel steepness index can be justi-
 fied by the context of a study. For example, Demoulin et al. (2015) expected
 215 the transient profiles they investigated to have varying concavities. As this was
 something that would not have been discerned by the segment fitting algorithm
 described by Mudd et al. (2014), they chose to visually select the segments.
 Here, the flexibility of these methods is advantageous, as it facilitates a more
 tailored approach to channel steepness index calculations. However, we might
 220 reasonably expect that different methods will produce different values of k_{sn} for
 the same data set, which again presents the problems associated with compari-
 son between studies and reproducibility.

Given the variety of ways k_{sn} can be calculated from χ -elevation data, it
 would be unreasonable to explain and evaluate each method individually within
 225 this paper. Instead, we will assess three broad approaches that cover the most
 popular approaches under current use. These are; splitting the χ -elevation data
 set using unconnected segments of equal sizes, splitting the χ -elevation data
 set according to sections of the profile that have the same gradient and thus
 channel steepness index, and methods which exploit the integral expression and
 230 use connected segments.

2.2.2. Channel steepness from equal sized segments

An obvious way to calculate channel steepness index for a stream network is
 to split the χ -elevation data into sections based on equal increments of either χ ,
 length or elevation. For each segment a line can be fitted through the χ -elevation
 data, which is described by the equation,

$$z(x) = z(x_b) + \left(\frac{k_s}{A_0^{\frac{m}{n}}} \right) \chi. \quad (11)$$

The gradient of each line is equal to the channel steepness index, divided by the reference area raised to the power of θ , or m/n . The y-intercept is the base level elevation, $z(x_b)$. For simplicity, $k_s/A_0^{\frac{m}{n}}$ can also be denoted U^* , a dimensionless value that represents relative uplift rate without necessitating an estimate of m/n .

The equal segment approach is useful as the size of segments can be controlled. Greater spatial resolution of channel steepness values can be achieved by using smaller segment sizes. However, smaller segments may be more susceptible to noise. Balancing this trade-off is important to ensure as much information is leveraged from the data set as possible.

However, choosing whether segments are equal in χ , elevation or length space impacts how the data set is sampled (Fig. 3). If equal elevation segments are chosen, then flatter sections of the profile will contain more data points than steeper sections. Likewise, segments made with a constant χ value will have fewer data points in the headwaters, where there are bigger differences in drainage area and χ from pixel to pixel, than in the lower reaches of the river. This makes upstream locations more susceptible to noise, as well as introducing bias. It is important to note that the smaller segments created by the constant χ or elevation method always sample the headwaters of stream networks. We may expect the natural noise to be highest in these areas, given that they tend to host steeper hillslopes that are more prone to failure, and have less stream power available to remove large boulders or debris flows from the channel (Lancaster & Grant, 2006; Schneider et al., 2008; Riebe et al., 2015).

Segments of equal length are useful for making channel steepness maps. However, in χ -elevation space, constant length segments are different sizes, which alters the resolution of the method at different points in the channel network. As shown in figure 3A, the constant length method has larger segments at high χ values, and so can only be used to interpret large scale variations in k_{sn} . At the lower end of the river profile, the segments become much smaller and so are susceptible to noise.

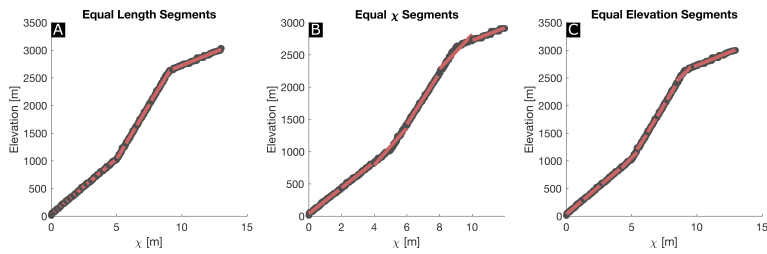


Figure 3: Synthetic profiles overlain by equal sized segments based on either length, χ or elevation. A - Length segments would appear equal on maps, however in χ -elevation space, segments sample an unequal number of points. In the headwaters, segments sample more points compared to in the lower reaches of the profile. B - Segments based on χ are equally sized in χ -elevation space, however on a channel steepness index map, downstream segments would appear longer than upstream segments. Some segments straddle changes in gradient, and so these changes will not be represented as sharply in the resulting model as they are in the data set. C - Segments based on elevation. Steeper sections of the river profile contain segments that have sample fewer points compared to flatter sections of the river. In the synthetic profile, the middle section is steeper and segments are shorter, reflecting this.

2.2.3. Unconnected segments of constant k_{sn} value

An equal increment approach can provide high spatial resolution, however, this is not always necessary in study areas where there are clearly defined segments of constant k_{sn} . In figure 3, there are two clear points at which the gradient of the χ -plot changes. If we use an equal increments approach, there will be segments that straddle the change of gradient (e.g., Fig. 3B). The gradient of these segments, and thus the k_{sn} values they record will have a value between the true values of the two channel sections. This therefore does not accurately represent the data set, introducing an error.

To improve the accuracy of segment fitting, we can split the χ -plot into the most likely constant k_{sn} segments. Segments are selected by choosing sections of χ -elevation data that appear to have the same gradient, corresponding to the k_{sn} value. This can be done by visually selecting segments (Demoulin et al., 2015), or by using a segment fitting algorithm, as described by Mudd et al. (2014). In this review, we will refer to this approach as the most likely segments approach.

Once the segments are selected, a regression line is fitted through the χ -elevation data of each segment. This gives each segment two parameters, a slope and a y-intercept, as described by equation 11. The segments therefore describe a simple, flexible, linear model of the stream network.

Whether the segments are created using an equal sized segment (section 2.2.2) or by taking sections of constant channel steepness, it is important to recognise that these segments are not connected. This can be advantageous, as it provides flexibility to the solution, however it can also be disadvantageous by introducing gaps or jumps between segments (Fig. 4). It is important to consider how these jumps are interpreted in terms of the underlying framework of the stream power model. Each point on a river network can be described in relation to its downstream points according to the integral expression (equation 10). As each point is connected to downstream points, there is no accounting for discrete jumps along the river profile. Should we wish to calculate erosion rates, uplift histories, or predict the χ -elevation relationship from the unconnected

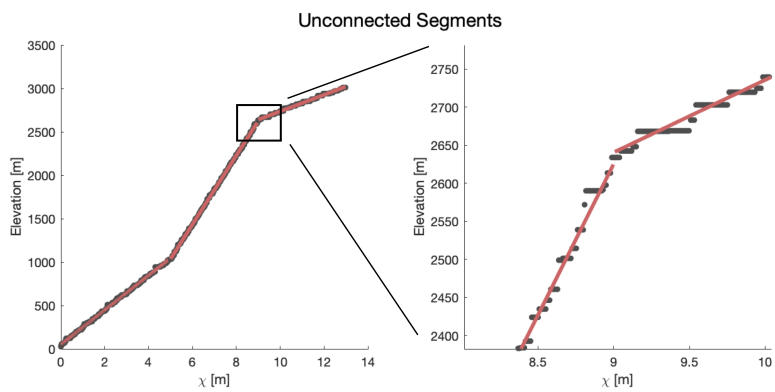


Figure 4: The synthetic χ -elevation data with the simplified model overlain. On the right, the figure is zoomed in on the gap between segments for clarity. The jump at the segment break is propagated through the reconstructed profile, leading to systematic residual values.

segments, the gaps between segments must be ignored. In terms of predicting the χ -elevation relationship, removing the jumps can lead to systematic over or under prediction along the profile. In figure 4, there is a positive gap between the lower reach segment and the upper reach segment. By ignoring this jump, the predicted elevations of the river nodes upstream of the jump will be lower than the observed elevation, in this case by approximately 20m (the size of the gap). The residual error between the predicted and observed elevations of upstream nodes caused by ignoring segments may increase with each jump that is ignored. For a complex river profile that may be characterised by multiple segments, each with an associated jump between them, the errors can grow to a magnitude of 100s of metres. This level of error limits our ability to use the predicted χ -elevation relationship to exploit additional information.

Having gaps between segments can also be problematic for interpreting the relationship between rock uplift and erosion rates. Consider a case where two neighbouring catchments have experienced the same rock uplift rate history. If there is a local feature that leads to the development of a waterfall in the first catchment but a steepened reach in the other, the waterfall would be identified as a break in slope in one, while the steepened reach may lead to an additional segment in the other. If channel steepness is plotted on a map, the waterfall would be completely unrepresented in one, but observed where the reach is steepened in the other. In this way, areas of steepening can be missed if it is more favorable to model these areas as discrete steps.

2.2.4. Channel steepness index from connected segments

The final category of methods used to calculate k_{sn} works directly with elevations as opposed to differences in elevations, which we will refer to as the connected segments approach. This method has been previously used to infer rock uplift rate histories (Roberts et al., 2012; Goren et al., 2014; Fox et al., 2015). The river profile is again split into segments of constant channel steepness index, however, the elevation of each point in a drainage network is defined by the summation of the downstream differences in χ multiplied by the

corresponding channel steepness index values. The elevation at a point, a , is thus represented by,

$$z_a = \sum_{b=1}^a (\Delta\chi)_b (ks_n)_b. \quad (12)$$

315 As the elevation of each data point is defined by previous segments, all the segments are connected and there are no gaps in the model. Closer to baselevel, more and more data points contribute to the estimate of channel steepness index at that segment, which also reduces model uncertainty. This is in contrast to other χ -based methods in which segments are treated separately.

A useful method to calculate ks_n based on equation 12 is to use a linear inverse scheme (Fox, 2019). First, the χ -elevation data set is discretised into small segments. This can be done by any reasonable means, but a simple way to demonstrate the approach is to imagine the pixels already present in a DEM. Using equation 12 similar equations can be written to describe the elevation of each pixel, and these can be combined into a matrix-vector product,

$$\begin{bmatrix} \Delta\chi_a & 0 & 0 \\ \Delta\chi_a & \Delta\chi_b & 0 \\ \Delta\chi_a & \Delta\chi_b & \Delta\chi_c \end{bmatrix} \begin{bmatrix} ks_a \\ ks_b \\ ks_c \end{bmatrix} = \begin{bmatrix} z_a \\ z_b \\ z_c \end{bmatrix} \quad (13)$$

320 where a , b and c represent pixels in the stream network, $\Delta\chi$ is the difference in χ between the downstream pixel and the pixel of interest, ks is the channel steepness index value between the downstream pixel and the pixel of interest and z is the elevation of the pixel of interest. Equation 13 takes the form,

$$\mathbf{A}\mathbf{k} = \mathbf{z}, \quad (14)$$

325 where \mathbf{A} is a matrix containing the increments of χ and is size 3x3 in this example, \mathbf{k} is a 3x1 vector of unknown channel steepness values and \mathbf{z} is a 3x1 vector of elevations.

Given that the χ values and elevations of each pixel can easily be extracted and calculated using a DEM, the unknown in equation 13 and 14 is \mathbf{k} , the vector of channel steepness index values. To calculate channel steepness, we therefore
330 solve equation 14 as so,

$$\mathbf{k} = \mathbf{A}^{-1}\mathbf{z}. \quad (15)$$

This equation forms the basis of a linear inverse method that has been used to calculate channel steepness index values from χ -elevation data (Goren et al., 2014; Fox, 2019; Fox et al., 2020).

Whereas other χ -based methods counter the effects of noise by fitting regressions and averaging points in segments, the linear inverse system described here fits a solution through as many data points as possible. This is advantageous as we are using as much of the information available, however, it can also make the solution susceptible to noise. A useful approach to handle the effects of noise is to perform the inversion with damping, or stiffness.

In our synthetic example (section 4.1), we introduce smoothness constraints that modify the system in equation 14 as follows,

$$\begin{pmatrix} \mathbf{A} \\ \alpha \mathbf{W} \end{pmatrix} \mathbf{k}_s = \begin{pmatrix} \mathbf{z} \\ \mathbf{0} \end{pmatrix} \quad (16)$$

where $\alpha \mathbf{W}$ is the damping matrix for \mathbf{k}_s .

\mathbf{W} is a negative Laplacian operator that calculates the second order spatial derivative of the parameters, \mathbf{k}_s . Solving \mathbf{W} multiplied by \mathbf{k}_s for 0 ensures that values vary smoothly in space, by forcing the curvature between the k_{sn} value of a pixel, and the k_{sn} values of its spatially adjacent pixels to be equal to 0.

The parameter α controls the importance of the weighting matrix to the solution. As α increases, the misfit associated with rough solutions also increases. In order to minimise the total misfit of the solution, the fit of the solution to the elevation data is sacrificed. In this way, α can be used to balance the trade-off between the smoothness of the solution and fit to the data. A suitable value for α can be determined using an l-curve, which graphically represents the trade-off between misfit and roughness (Hansen, 1992). A more detailed explanation of a weighted linear inverse system used to calculate k_{sn} values is provided by Fox (2019).

Multiple approaches exploit similar concepts (Roberts & White, 2010; Roberts et al., 2012; Goren et al., 2014; Rudge et al., 2015; Fox et al., 2020), although implement damping differently. In Fox et al. (2015) the connected segment approach as described here was implemented, however, a non-linear algorithm
360 was used in which the discretisation is flexible and the lengths, and number, of different segments are free to vary using a change point algorithm. The key difference between these methods and other χ -based methods is that segments are based on an integration, and so are connected. In the synthetic problem, we use a damped linear inverse scheme as described by equation 16, discretising
365 the synthetic data using a small $\Delta\chi$ value. In reality, the segment lengths can be chosen using any suitable method as previously described (Sections 2.2.2 and 2.2.3).

3. Methodology for evaluating approaches

3.1. The Synthetic River Profile

370 Having outlined the key approaches to calculating channel steepness index in section 2, we now evaluate the accuracy and limitations of each approach. A suite of MATLAB algorithms have been written to replicate the approaches explained above, and these are used to calculate channel steepness from synthetic and real world data sets. The algorithm for each approach is tested using
375 a synthetic, 1-D river profile, which replicates a DEM-derived river profile. The profile was created using a vector of river nodes, that are separated by equal distances, representing the size of a pixel in a DEM. Each node is given an upstream area value based on Hack's Law (Hack, 1973) and a χ value, based on equation 10. Elevations are assigned to each node using equation 12, al-
380 lowing the profile to be created using known values of channel steepness index. The advantage of using a synthetic profile is that we can directly compare the values calculated from each method to the known values of channel steepness index, allowing the accuracy of each methodology to be assessed. The complexity of the profile can also be changed, so that different sections have different

385 channel steepness values. This is useful for testing the limitations of different approaches.

To replicate a real world scenario, we introduce artificial noise to the synthetic profile by increasing the elevation of a given node by a random number between 0 and the ‘noise-level’. Where the introduced noise causes a downstream node to be higher than the adjacent upstream node, both nodes are
390 given the same elevation to ensure the profile mimics that of hydrologically conditioned, DEM-derived profile. The level of noise and the complexity of the profile can be increased and decreased to explore the limitations of each method. Slope-area analysis (section 2.1.1) is well known to be susceptible to
395 noise (Wobus et al., 2006; Roberts et al., 2012; Perron & Royden, 2013), as touched upon in section 2.2. In order to derive meaningful results from the synthetic dataset using slope-area analysis, the level of noise is reduced to a maximum of 5m for this analysis. Furthermore, the profile is created with just one channel steepness index value. The other methods, which are based on the
400 integral approach (Section 2.2), are all examined using a more complex synthetic profile, comprised of three sections with different channel steepness index values. This synthetic profile also has been created with a higher noise level of 10m, representing a more realistic, DEM-derived data set.

For each method, the calculated channel steepness index values are used to
405 reconstruct the river profile, using equation 12. The residuals between the reconstructed profile and the synthetic profile are then calculated, facilitating some level of quantification of the potential errors inherent in different methodologies.

3.2. *Real world data sets*

To evaluate the approaches in 2-D, we use a data set from the Sierra Nevada.
410 We extract the Cottonwood Creek river network from a 30m SRTM DEM (Farr et al., 2007) using TopoToolbox (Schwanghart & Scherler, 2014), and use the aforementioned algorithms to calculate channel steepness index values. These values are then plotted as channel steepness index maps, highlighting how various approaches are better suited to discerning spatial variation compared to

415 others. Comparing channel steepness index maps of the same area, created using different approaches, demonstrates how spatial variation in channel steepness can vary as a function of the chosen approach.

3.3. *Beyond Channel Steepness Index*

If the approaches used to extract channel steepness are closely related to the
420 integral approach, information can be combined from neighboring tributaries and channel steepness values can be extrapolated. Parameters such as surface uplift can be incorporated into the analysis, lending more depth to results and aiding their interpretation. To test these approaches, we use a larger data set that incorporates many river networks across the southern Sierra Nevada,
425 including the Kern river. This data set is again derived from a 30m SRTM DEM (Farr et al., 2007) and extracted using TopoToolbox (Schwanghart & Scherler, 2014). River profiles across this area should contain a variety of spatio-temporal signals, reflecting the complex uplift and climate history recorded in the area (Wakabayashi, 2013; Moore & Moring, 2013; Krugh & Foreshee, 2018;
430 Beeson & McCoy, 2020) and significant spatial variation in lithology present today (Jennings et al., 2010). Unpicking these signals is difficult, which is why we use a method designed to exploit additional information, and reveal non-steady surface uplift. This study area is representative of the tectonically active landscapes everywhere, with regards to the non-uniform distribution of
435 precipitation, lithology, and tectonic forcing.

4. Results

4.1. *Synthetic Profiles*

The channel steepness values for the synthetic profile, as calculated by four different approaches (pixel by pixel, constant length segments, most likely seg-
440 ments and connected segments) are displayed in figure 5. Comparing the values of channel steepness in the histograms (Fig. 5 C, G, K, O) to the values used to create the profile allows us to assess the accuracy of each approach. Furthermore, any systematic bias or error inherent in each approach can be discerned

with the aid of the reconstructed profiles(Fig. 5 B, F, J, N), and the residual
445 histograms (Fig. 5 D, H, L, P).

4.1.1. Accuracy

The synthetic profile and thus the χ -plot have three distinct sections created using three values of channel steepness. The lower reach was created with a value of 200, the middle reach with a value of 400, and the upper reach with a value
450 of 100. An accurate method would therefore produce a histogram with three peaks, at 100, 200 and 400.

Of the four approaches tested, the pixel by pixel approach appears to be the least accurate. There are more river nodes with channel steepness values at 100, 200 and 400, however, there is also a high frequency of values between and either
455 side of these values (Fig. 5C). As this method relies on slope, or differences in elevation of adjacent nodes, calculated channel steepness values deviate from the true value with the addition of noise. Where noise causes the difference in elevation of two adjacent nodes to be greater than the true signal that is expected, the channel steepness value that is calculated is also greater. As the
460 calculation is performed on a pixel by pixel basis, wherever adjacent pixels are affected by noise, so to is the calculated channel steepness value. Even in this example, where a sliding window smoothing algorithm is passed over the river node elevations, noise is still present, reducing the accuracy.

The equal segments approach, where segments of equal length are used to
465 average the gradient is more accurate than the pixel by pixel approach, but less accurate than the most likely segments approach. The channel steepness index histogram for the equal segments approach clearly has three peaks at the true channel steepness values (Fig. 5G). These peaks are less dispersed than in the pixel by pixel histogram (Fig. 5C), indicating that there is less variance in the
470 calculated values. Errors are introduced into this method where large segments sample a change in channel steepness that occurs over a small lengthscale (fig. 4), and where short segments in the lower reaches become susceptible to noise.

The two most accurate methods are the most likely segments approach (Fig.

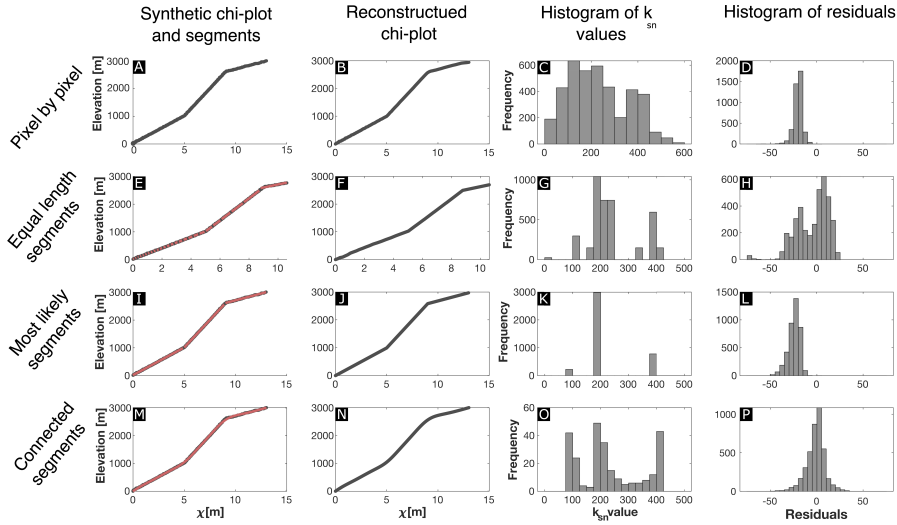


Figure 5: Results from the synthetic profile analysis. Row 1 (A-D) shows results for the pixel by pixel approach (section 2.1.2). Row 2 (E-H) shows results for the equal sized segment approach (section 2.2.2). Row 3 (I-L) shows results for the most likely segments approach (section 2.2.3). Row 4 (M-P) shows results for the connected segments approach, which uses the damped linear inverse scheme described in equation 16 (section 2.2.4). A - a χ -plot as created from the synthetic river profile. This profile has had noise artificially introduced as described in section 3.1. E, I, M - the same synthetic profile as shown in A, however the segments or solution has been overlain in red. E - note the equal length segments decrease in size in χ -space towards the lower reaches of the river profile. This can introduce a sampling bias, and alter the resolution of the approach on different parts of the river. B, F, J, N - the reconstructed χ -plots for each of the approaches. The χ values for each point on the synthetic river are already known, and the elevation is predicted from the calculated channel steepness index value and the differences in χ between each node, as described by equation 12. C, G, K, O - a histogram of the calculated channel steepness index values for each approach. D, H, L, P - The residual values between the reconstructed profile and the actual profile. The pixel by pixel(D), and most likely segment approaches (L) systematically underpredict the elevations of points on the river. The equal segments approach has values that are residuals that are positively and negatively skewed, and have a non-normal distribution. The connected segment approach (P) has residuals centred about 0.

5K) and the connected segments approach (Fig. 5O). The channel steepness
475 histograms for both of these show clear spikes at 100, 200 and 400. A small
number of the discretised sections of the connected segment approach have val-
ues that fall outside of the true values. This is caused by discretised sections that
sample the sharp contrast in channel steepness. Similar to the equal segments
approach, the discretised sections that straddle a change in channel steepness
480 index will calculate a value between the two true values. However, in the con-
nected segment approach which uses a damped linear inversion, sections that
sample the change in channel steepness also influence adjacent sections as there
is a requirement for the solution to be smooth. On the other hand, as the
changes in channel steepness are known in synthetic sample, the most likely
485 segments approach perfectly samples the profile. Hence, there are no segments
with inaccurate values of channel steepness. In real data sets, the changes are
not known, and profiles are often more complex. In these cases, we would ex-
pect some inaccuracy caused by averaging complex profiles into segments with
constant channel steepness values.

490 4.1.2. Residuals

The residual values between the true profile and the reconstructed profile
are plotted as histograms in figure 5D, H, L, P. The first observation that can
be made is that the connected segment approach is the only method that has
residuals normally distributed around 0. For the other three methods tested,
495 the residuals are skewed to one direction, or non-normally distributed. In the
pixel by pixel approach, the smoothing algorithm used may have introduced
an error that causes elevations to be systematically underpredicted. For the
equal segments approach and most likely segments approach, differences be-
tween predicted elevations and observed elevations are more likely to be caused
500 by the gaps between segments, as discussed in section 2.2.3. If a gap in a down-
stream section causes the elevation of a river node to be less than the true
value, the mismatch in elevation is propagated through the rest of the profile as
it is reconstructed, and vice versa. In this way, residual values can be skewed

either negatively or positively. For the connected segment approach however,
505 discretised sections are connected, and every point is given equal priority in
the solution. Downstream segments do not impact the elevations of upstream
segments, and the solution and reconstructed profile stay tight to the observed
profile.

4.2. Slope-Area analysis

510 To demonstrate the susceptibility of slope-area analysis to noisy data, we
perform slope-area analysis on three synthetic profiles, created using different
noise levels (Fig. 6). The noise levels of all three of these profiles is much lower
than might be expected from a DEM data set.

At noise levels that are almost imperceptible in the synthetic river long pro-
515 files, the channel steepness index values calculated from slope-area analysis are
inaccurate. In figure 6A, a noise level of 0.1m results in an error of approxi-
mately 5% (the true value of k_s is 200). However, increasing the noise level to
just 1m (Fig. 6D), half that associated with DEM acquisition errors (Short-
ridge & Messina, 2011), the error on the channel steepness value is greater than
520 50%. Beyond this, calculating a channel steepness value becomes impossible
(Fig. 6F). Whilst this observation has been made previously, (Roberts et al.,
2012), we include slope-area analysis in this review for completeness.

4.3. Assessing Spatial Variation using k_{sn} maps

One key application of channel steepness index is to assess spatial variation
525 in relative rock uplift rates, typically done by creating channel steepness index
maps. As will be demonstrated, different approaches create different maps for
the same data set, and there are various considerations that should be taken into
account before choosing an approach. To assess these considerations, we test
the pixel by pixel, equal length segments, most likely segments and connected
530 segment approaches on a real world data set from the Sierra Nevada.

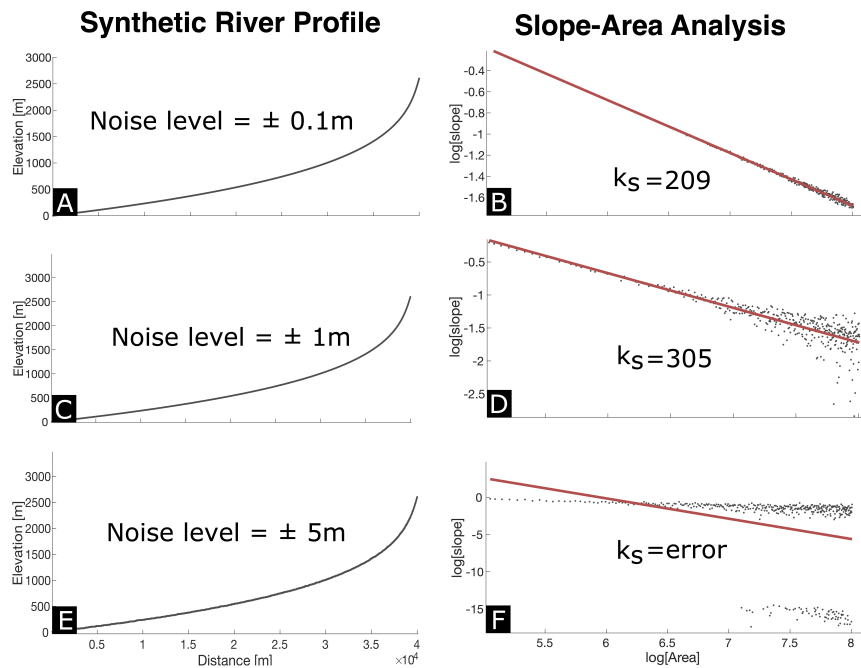


Figure 6: A, C, E. Synthetic profiles created with different amounts of synthetic noise. Profiles C and E have noise levels on the same order of magnitude as noise introduced by errors in the DEM. Typically DEMs would contain more noise from additional sources such as geomorphic noise and man-made objects (Schwanghart & Scherler, 2017). B, D, F. Slope-area analysis performed on each synthetic data set. As noise increases, there is a greater error associated with the calculated k_s value. At $\pm 5\text{m}$ of added noise (F), fitting a line through the data becomes trivial, and the k_s value calculated is an imaginary number. The 5m noise level profile contains less noise than would be expected for DEM-derived data sets.

4.3.1. Cottonwood Creek

Cottonwood Creek is a short river located near Round mountain (Fig. 7), that runs perpendicular to, and cuts across the Sierra Nevada Frontal Fault (Le et al., 2007). Although it is a relatively small catchment, there is considerable spatial variation in channel steepness index, which makes it an ideal area to compare different approaches to making maps. Once the channel steepness index maps from different approaches are compared and contrasted, they will be used to investigate the factors driving this variation.

To make channel steepness index maps of this catchment, we first extract Cottonwood Creek from a 30m SRTM DEM (Farr et al., 2007), using TopoToolbox (Schwanghart & Scherler, 2014). A filter is used so that only river nodes with an upstream area greater than 1×10^6 pixels are included in the data set. Channel steepness index is then calculated for river nodes using different approaches described in the previous section, before the values are plotted on a map.

4.3.2. Smoothed pixel by pixel approach

A popular approach to making channel steepness index maps is to use a pixel by pixel approach as described in section 2.1.2. Although a normalised channel steepness index map could be calculated using the raw extracted slope – area data, this tends to result in anomalous k_{sn} values that occur across short length scales (Fig. 8A). The anomalous values can obscure the true spatial pattern of channel steepness, and the resulting maps can be difficult to interpret. Given the goal of making a channel steepness map is to allow researchers to visualise the most prominent spatial variation in k_{sn} across an area, it is preferable to introduce a smoothing algorithm.

However, many different smoothing algorithms exist, from moving averages to interpolations, and they can be implemented in different ways. Commonly when making channel steepness maps, moving windows are used to smooth either the river elevation data, or the resulting channel steepness values (Fig. 8B, Vanacker et al., 2015; Basilici et al., 2020; Campforts et al., 2020; He et al.,

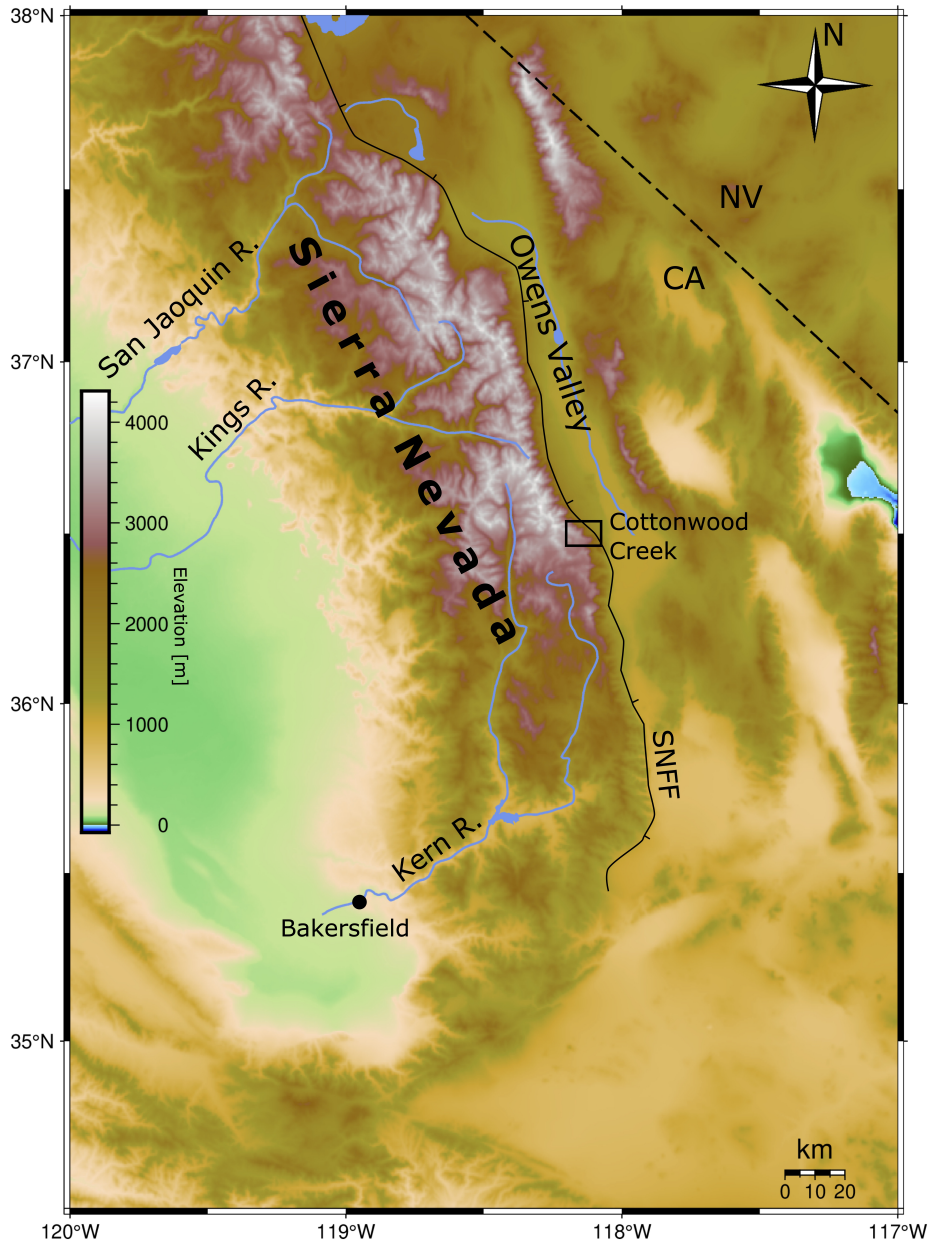


Figure 7: A map of the southern Sierra Nevada, including the Kern, Kings and San Joaquin rivers. The location of the Cottonwood Creek catchment is shown by the black rectangle. The Sierra Nevada Frontal Fault system (SNFF) runs down the eastern margin of the range, cutting across Cottonwood Creek.

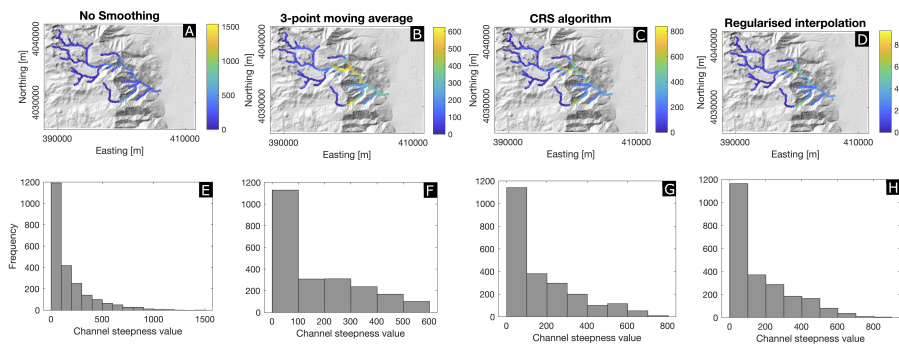


Figure 8: A-D - Four channel steepness maps created using the same Cottonwood Creek data set. E-H - histograms of the channel steepness values of each node on the river. Although the overall pattern of channel steepness is similar in each map, there are discrepancies within the absolute values of k_{sn} calculated. The similarities of the four maps mean that the choice of smoothing algorithm may not be important to observe large scale changes in channel steepness. However, given that the absolute values differ, there are difficulties deciding which solution represents the most accurate channel steepness index values. Choosing which approach and map reflects the true values can be difficult without prior knowledge of the area, and given maximum values can vary by an order of magnitude, how can we be sure the k_{sn} values are even representative of the relative uplift rate in the area?

2020; Racano et al., 2021). In our analysis, we calculate channel steepness index values using four variations of smoothing (Fig. 8). One map is created from raw slope-area data, without the use of smoothing (Fig. 8A). Two of the maps are created using different smoothing algorithms passed over the river network elevation data. One algorithm is based on regularised interpolation (Fig. 8D),
565 and the other is the constrained regularised smoothing algorithm developed in TopoToolbox (Fig. 8C, Schwanghart & Scherler, 2014, 2017). Finally, one map is created using a 3-point moving average passed over the k_{sn} values themselves (Fig. 8B). In reality, the channel steepness maps created using the 3-point
570 moving average are the same regardless of whether smoothing is performed on the elevation data or the channel steepness values. However, the interpolation algorithm used here uses a stiffness penalty. As the values of elevation and channel steepness index differ by an order of magnitude, using the same value for the stiffness penalty will result in different outcomes based on whether the
575 smoothing is performed on the elevation data or the channel steepness values.

The different smoothing techniques tested here all produce maps with similar patterns of channel steepness (Fig. 8A-D). In each map, there is an upstream section of the river network with low values of channel steepness, and a downstream section close to the mountain front with higher values. The broad
580 pattern of channel steepness is therefore consistent across techniques. However, tangible differences between the calculated values of channel steepness exist, as evidenced by the histograms of channel steepness (Fig. 8E-H). The maximum value of channel steepness from the unsmoothed map is more than double the value from the map that was smoothed using a 3-point moving average. There
585 are also different distributions of values of channel steepness across each methodology. The issue here is deciding which set of values is most accurate. If we are using channel steepness index to quantitatively examine an area, e.g to correlate measurements of catchment wide erosion rates from cosmogenic nuclides to larger areas with greater spatial resolution (Safran et al., 2005; DiBiase et al.,
590 2010; Cyr et al., 2010, 2014; Scherler et al., 2014; Harel et al., 2016), or calibrate uplift rates and uplift histories (Roberts et al., 2012; Goren et al., 2014), using

a set of values from one approach over another will produce different results. In this case, it is not clear which smoothing methodology is most representative.

As is expected, different approaches to smoothing have different advantages and disadvantages. In the case of smoothing the topography first and then calculating channel steepness values, for example, unexpected artefacts may be generated. In particular, if the river network is in steady state, tributaries may have very different slopes to trunk channels. Even if channel steepness is uniform, the elevation differences at confluences may be very abrupt (Playfair's Law, Playfair (1802)). Smoothing the topography artificially removes these abrupt changes in elevations, introducing artefacts. It is possible to not smooth across confluence junctions, and infer channel steepness in the trunk stream and tributaries separately. This, however, does not exploit the fact that the close proximity of fluvial pixels with very different slopes and areas provide tight constraints on channel steepness.

To determine the nature of errors introduced by some of these smoothing algorithms, river profiles are reconstructed using the calculated channel steepness values. The residuals between reconstructed profiles and the actual profiles are then calculated, as was done with the synthetic data set. These have been plotted on a histogram (Fig. 9), so that potential errors can be assessed. One important observation from this histogram is that apparent errors can change depending on the smoothing methodology implemented.

The three smoothing algorithms tested in our study all introduce different errors to the channel steepness index calculation, as demonstrated by the skewed residual distributions in figure 9. As the residuals are skewed by different amounts depending on the smoothing approach used, it can be difficult to account for the error introduced by each method. Similarly, comparing values across studies that use the pixel by pixel approach, but different smoothing techniques, may also be difficult, owing to the different errors that need accounting for. Even when the same smoothing algorithm is used, results can vary depending on the various parameters, such as stiffness penalties, that can be chosen.

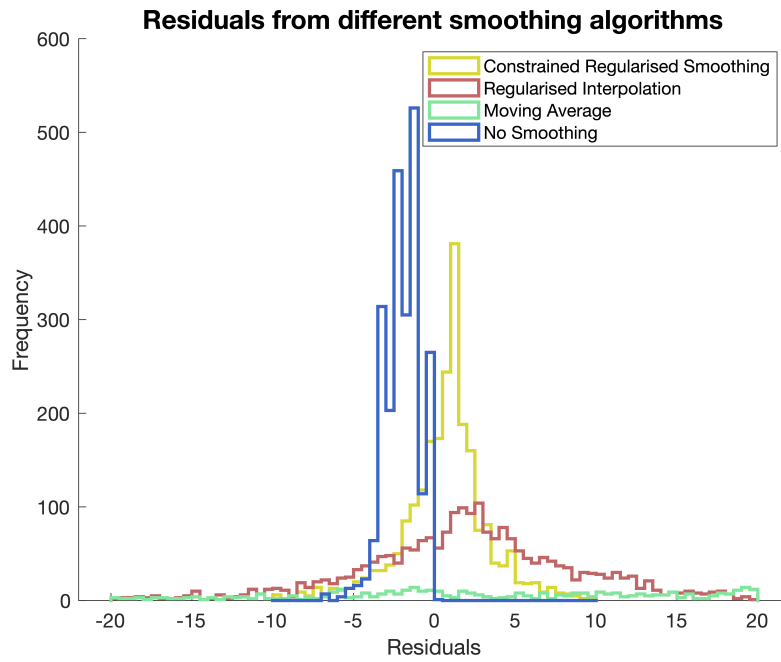


Figure 9: Histograms of the residual values for 3 different smoothing algorithms and an unsmoothed reconstructed profile. The residuals have different values, which can make accounting for bias difficult. Values of residuals can vary depending on the type of algorithm used, when smoothing is performed (before or after k_{sn} calculation), and which parameters are used in the algorithm.

4.3.3. χ -based approaches to k_{sn} maps

χ -based approaches have an advantage over approaches that use slope data, by working directly with elevation. The χ -elevation data set contains less noise, which generally leads to more accurate results. Furthermore, as there is a reduction in the effects of noise, smaller signals can be detected, owing to a reduction in the noise to signal ratio. Channel steepness index maps created using χ -based methods can achieve high resolution, without sacrificing accuracy of calculated values.

As explained in section 2.2, multiple approaches exist for calculating channel steepness index from the integral approach. For example, within the equal sized segment approach (section 2.2.2), the segment size could be based on length, elevation or χ value. Choosing which dimension to work in is not arbitrary, as it can change the pattern of the resulting channel steepness index map, and the absolute values of channel steepness index calculated (Fig. 10).

To calculate channel steepness index values for Cottonwood Creek, we use the same data set as used in pixel by pixel approach. To calculate χ values, we assume a concavity index of 0.3, based on the value used by Goren et al. (2014) for the proximal Inyo range. Channel steepness values were then calculated from this χ -elevation data using similar algorithms to those deployed on the synthetic profile. The χ -elevation data set was split up into segments of equal length (Fig. 10A), elevation (Fig. 10C), and χ (Fig. 10B), as well as unequal segments based on sections that have constant k_{sn} values (Fig. 10D). Regressions were fit through these segments, and the gradients of these were taken as the U^* values, proportional to channel steepness index values.

To plot the values on a map, we follow the methods described by Mudd et al. (2014) and Wahyudi et al. (2021). For each approach, segments are defined on a χ -plot prior to the calculation of channel steepness or U^* . The nodes within a segment are given the calculated value of U^* for that segment, and are then plotted on the river network.

Despite two-fold differences in the maximum channel steepness value when

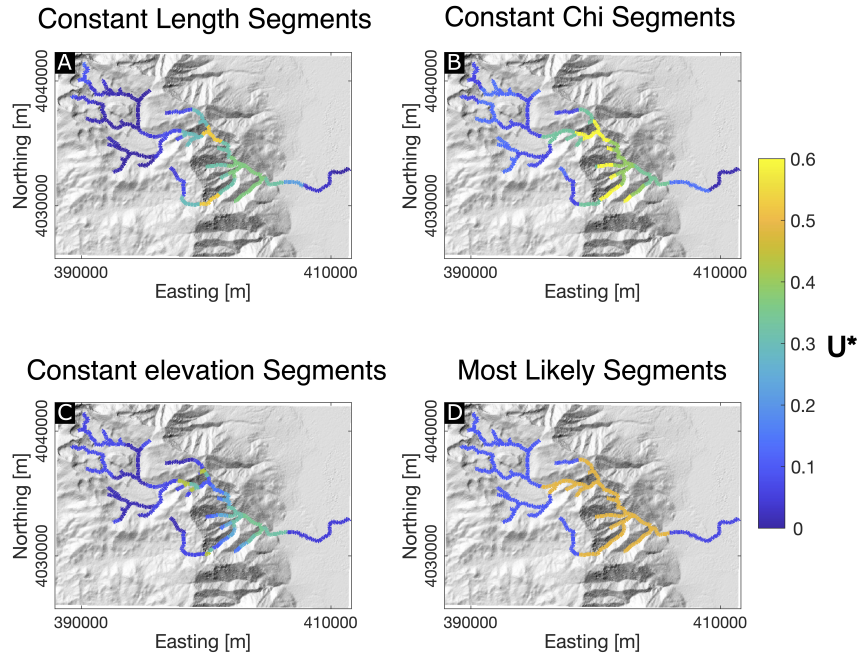


Figure 10: Channel steepness index maps of Cottonwood Creek, created using different χ -based approaches. A - channel steepness map created using constant length segments. Segments are the same size across the map. B - channel steepness map created using a constant length segments. Segments in the headwaters tend to be smaller, and sample fewer data points. C - channel steepness map created using a constant elevation segments. Steepest sections of the channel are sampled more frequently by segments. D - channel steepness map created by visually selecting segments with a constant k_{sn} value. There are three segments selected using this approach, which limits our ability to infer spatial drivers of channel steepness index, if they are present.

comparing the four maps (Fig. 10), the range of reported channel steepness values from the χ -based methods is less than with the pixel by pixel approach. The calculated channel steepness index values from χ -based approaches are within the same order of magnitude, as opposed to the different values created using the pixel by pixel approach (Fig. 8). Similar to the pixel by pixel approach however, the pattern of channel steepness is approximately the same across all four χ -based approaches (Fig. 10). Each χ -based approach picks out low channel steepness values in the upper reaches, and higher values in the lower reaches. As there is a smaller range of channel steepness index values calculated from the four χ -based approaches compared to the pixel-by-pixel approach, there is less uncertainty when using those values in quantitative studies of erosion and uplift rates. This is an important consideration when choosing a specific methodology for a study.

Shorter segments can be selected when using chi-based approaches compared to approaches based on slope, as elevation data contains less noise compared to slope data. When plotted on a map, shorter segments provide greater spatial resolution, facilitating the detection of smaller signals present within the data set, such as those associated with changes in lithology at geological contacts. To examine whether lithology influences the pattern of channel steepness index within the small Cottonwood Creek catchment, we overlay the length segments channel steepness index map with a geological map (Du Bray & Moore, 1985). If lithology were exerting a strong control on channel steepness index, we would expect to see sharp contrasts in channel steepness index at lithological boundaries. This spatial pattern is not reflected in the channel steepness map (Fig. 11), and so an alternative interpretation must be sought.

4.4. *Transient signals of uplift rate*

Examining the χ profile of Cottonwood Creek upstream of its intersection with the Sierra Nevada Frontal Fault, two sections representing two channel steepness values can be observed (Fig. 12). The upper reaches flow over a low relief, high elevation landscape, whereas the lower reaches flow through incised

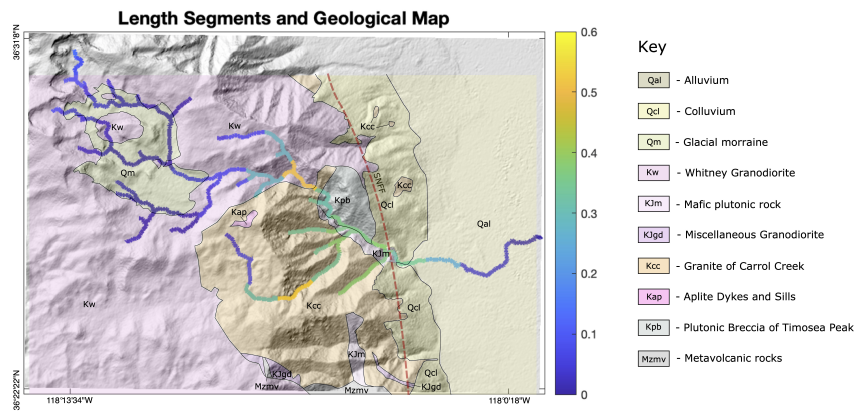


Figure 11: The length segment channel steepness index map overlain on a geological map (modified from Du Bray & Moore (1985)). Even within the small Cottonwood Creek catchment, there is significant variation in lithology. However, this does not appear to strongly influence variation in channel steepness index. The same is true for structural features such as the Sierra Nevada Frontal Fault (SNFF).

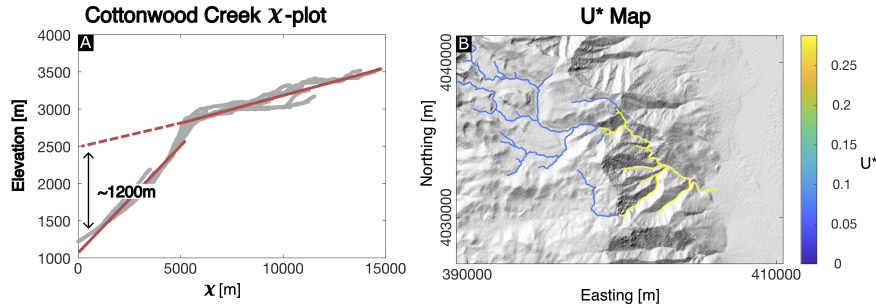


Figure 12: Left - a χ -plot for the extracted Cottonwood Creek network. Two segments have been picked out, potentially representing temporal variation in uplift rate. The segment that samples the upper reach of the river has been extrapolated to give an estimate on the amount of recent surface uplift. This estimate is approximately 1200m. Right - the U^* values as calculated from the segments are shown on a map. As expected, the low relief surface has a lower U^* value than the incised Sierra Nevada escarpment.

canyons on the Sierra escarpment. It would be reasonable to assume that the low relief topography represents an advected palaeo-landscape, that has yet to
 685 be brought into equilibrium with the higher uplift rate observed in the lower reaches. The k_{sn} value of the upper section is relatively low, whereas the lower section has a higher k_{sn} value. This indicates that there has been an increase in the relative uplift rate in this part of the Sierra Nevada.

Assuming the upper reaches of Cottonwood Creek preserve a relict land-
 690 scape, we can estimate the surface uplift that has been caused by the recent increase in relative uplift rate. Extrapolating the upper segment of the river to the elevation axis, we observe that the increase in relative uplift rate evidenced in the lower reaches has resulted in approximately 1200m of incision (Fig. 12). Assuming the upper reaches of the landscape have been eroding
 695 at a constant rate despite the change in rock uplift rate, this figure also represents the amount of surface uplift that has occurred at this location along the Sierra Nevada Frontal Fault. This is broadly consistent with estimates of surface uplift from previous studies (Wakabayashi & Sawyer, 2001; McPhillips & Brandon, 2012; Wakabayashi, 2013; Beeson & McCoy, 2020), but this is an
 700 isolated estimate that taken alone, does not provide concrete evidence for this

event as other processes could shape this river. Furthermore, because it is only from a single river, this estimate cannot be used to infer a driving process.

To better understand the history and drivers of surface uplift across the Sierra Nevada, we need to examine a larger area. The pixel by pixel approach
705 can be used to calculate channel steepness index over large areas relatively quickly. However, as channel steepness index represents a combination of both uplift and erosion, this approach is unable to resolve surface uplift. Above we explain how surface uplift can be inferred using a χ -based segment approach for a single river (Fig. 12). However, this approach is limited when expanded
710 to multiple river networks. Surface uplift can only be calculated for each individual river network. Over different river networks, there is spatial variation in rock uplift and erosion, and geomorphic noise. This inevitably causes channel steepness values to vary, leading to spatially varying estimates of surface uplift. Where the value of surface uplift of adjacent river networks is different, it is
715 unclear how the two values should be averaged. If we believe the two values are different due to some signal or driver, how do we map the change from one network to the other? Alternatively, noise could be responsible for the variation, in which case an average of the two values assigned to both networks might be more appropriate. Because each network is examined separately, there is no
720 way to incorporate information from across large areas.

In the next section, we modify the linear inverse scheme to incorporate information from across a large area with multiple river networks to create a map of channel steepness and surface uplift. Channel steepness index and surface uplift maps can both be created using this approach, providing better constraints of
725 the drivers of rock uplift and erosion across the Sierra Nevada. This would be difficult to infer solely from channel steepness index.

4.5. Further exploiting the forward model - a case study from the Sierra Nevada

4.5.1. The southern Sierra Nevada

The Sierra Nevada is a northwest trending, 600km long mountain range located in eastern California. In a broad sense, the Sierra Nevada consist of the
730

Sierra Nevada Batholith, part of an exhumed Mesozoic arc that behaves as a rigid, westward tilting block (Saleeby et al., 2013; Cao et al., 2015). The mountain range has an interesting and debated uplift history, owing to its unusual structure. Despite supporting elevations of over 4000m, geophysical evidence
735 suggests the Sierran Nevada crust is relatively thin (\sim 35-40km) (Wernicke et al., 1996; Frassetto et al., 2011). To explain this discrepancy, many studies point to delamination of an eclogitic crustal root beneath the Sierra Nevada, and support from upwelling, buoyant mantle (Ducea & Saleeby, 1998; Saleeby et al., 2013; Yu et al., 2020; Ryan et al., 2020).

740 Despite geological and geophysical evidence for delamination and the presence of hot buoyant mantle beneath the Sierra Nevada, controversy remains as to whether this process is responsible for an episode of late Cenozoic uplift. The timing, mechanism, magnitude and even the existence of this phase of uplift continues to be debated. Late Cenozoic uplift has been inferred from geomorphological evidence (Wakabayashi & Sawyer, 2001; Wakabayashi, 2013; Clark
745 et al., 2005; Figueroa & Knott, 2010), GPS data (Hammond et al., 2016) and thermochronology (McPhillips & Brandon, 2012; Cecil et al., 2014). However, these findings contradict isotope data and evidence from the sedimentary record that suggests Sierra Nevada relief has been present since at least the Eocene,
750 likely forming due to subduction tectonics in the Cretaceous (Poage & Chamberlain, 2002; Cassel et al., 2012, 2014). If recent surface uplift has occurred, it is unclear whether this was mantle-driven (Saleeby et al., 2013; Krugh & Foreshee, 2018) or caused by westward tilting of the rigid Sierra Nevada block (McPhillips & Brandon, 2012; Beeson & McCoy, 2020).

755 To investigate recent surface uplift in the southern Sierra Nevada we examine the rivers of the southern Sierra Nevada, including the Kern River. The Kern river is the southernmost major river of the Sierra Nevada, flowing southwards from Mt. Whitney to Lake Isabella, before changing course to the west and flowing out of the Sierra Nevada through Bakersfield. In its upper reaches,
760 the Kern flows through the high-elevation, low relief topography of the Kern plateau (Clark et al., 2005; Krugh & Foreshee, 2018), the same feature that

hosts the headwaters of Cottonwood Creek. In the previous section (section 4.4), we demonstrated how this low relief palaeo-surface could be used to estimate surface uplift at one location from a single χ -plot. Here we extend this approach
765 to incorporate information from a large area, to calculate surface uplift across the entire southern Sierra Nevada.

4.5.2. Approach

As with the previous example, MATLABs TopoToolbox (Schwanghart & Scherler, 2014) is used to extract a stream network from a SRTM 30-meter
770 resolution DEM of the southern Sierra Nevada. This network consisted of all streams with an upstream area greater than 5×10^6 pixels, upstream of the limit of the southern Sierra Nevada range. The area is then discretised into $2\text{km} \times 2\text{km}$ pixels, which incorporate the corresponding nodes from the stream network. These pixels can be thought of as analogous to the segments in the
775 previous section. (Please note that we use nodes to describe the river network and pixels to describe the discretisation). In the solution, nodes within a single pixel are forced to have the same value of channel steepness and the same value of surface uplift, but the value of the channel steepness and surface uplift varies from pixel to pixel. The amount by which values of channel steepness and
780 values of surface uplift can change between adjacent pixels is controlled by the weighting matrix. Values of χ and elevation for the river network are then incorporated in a linear inverse system, which is solved using a least squares approach. The methodology builds on the concepts described in section 2.2.4 and Fox (2019); Fox et al. (2020). The advantage of using this approach is
785 that as much of the available information is used to inform the solution. This contrasts to other methods in which signals may be lost due to averaging and smoothing.

The approach we use for the southern Sierra Nevada differs from that described in section 2.2.4 due to the inclusion of a surface uplift parameter. This
790 modifies equation 12, and the system of equations to be solved to the following,

$$z_i - B.L. = \sum_{j=1}^i (\Delta\chi)_j (k_{sn})_j + S.U._i, \quad (17)$$

where $B.L.$ represents common base level for the river network, and $S.U._i$ is the surface uplift at the i^{th} pixel. Equation 17 forms the basis of the system of equations to be solved, represented by,

$$\begin{pmatrix} & \mathbf{A} & \\ \alpha\mathbf{W} & & \cdot \\ \cdot & & \lambda\mathbf{W} \end{pmatrix} \begin{pmatrix} \mathbf{k}_{sn} \\ \mathbf{S.U.} \end{pmatrix} = \begin{pmatrix} \mathbf{z} \\ \mathbf{0} \\ \mathbf{0} \end{pmatrix} \quad (18)$$

where we have now introduced an additional damping term, $\lambda\mathbf{W}$, to control the smoothness of the surface uplift solution.

Solving this system for different values of α and λ provides different possible solutions. To guide our choice of solution, an L-surface for the misfit is produced. The chosen solution is selected as it has a reasonable value of misfit of approximately 100m, suggesting the model is balanced between fitting the data and dealing with noise (Parker, 1994; Richards et al., 2016; Fox et al., 2020).

4.5.3. Results

Our chosen solution shows that across the southern Sierra Nevada, at least 0.7-1.7km of surface uplift has been recorded within river profiles. Given the response time of river profiles to changes in uplift (Whittaker & Boulton, 2012), it is reasonable to assume this represents a cumulative signal of late Cenozoic uplift although rates may have varied in space and time. In the north of the map, there is increasing surface uplift from the western edge of the Sierra Nevada to the east. This provides evidence for westward tilting of the Sierra Nevada, in which there would be greater surface uplift further from the hinge of the tilt. However, as we move south the peak surface uplift values shift westward from the edge of the range. Instead of a clear gradient of surface uplift from one side to the other, maximum surface uplift values appear in the middle of the range. Rather than a tilting signal, there is fairly uniform surface uplift of

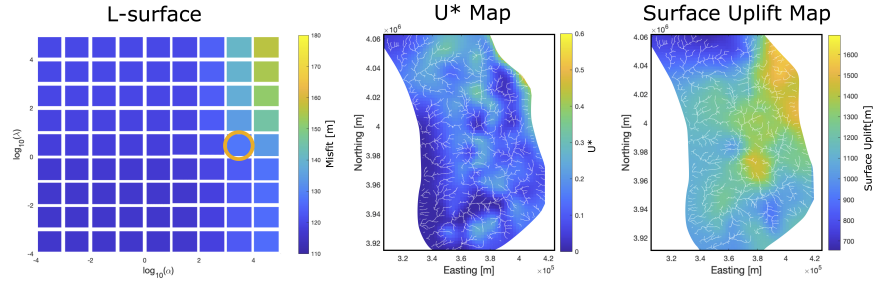


Figure 13: A - an L-surface showing the model misfit at different values of α and λ . The solution shown here was solved using the parameter values of the square in the orange circle. B - The U^* map of the southern Sierra Nevada. These U^* values are used to calculate the surface uplift experienced in this area. Most values are similar to the values calculated for Cottonwood Creek in the previous example. C - A surface uplift map of the southern Sierra Nevada. Moving from north to south, peak surface uplift values appear to shift from the eastern margin of the range to the centre of the range.

approximately values of 1300m across the southernmost portion of the Sierra Nevada. 815

The advantage of using the connected segments approach is that the model uncertainty is lower than for the unconnected segment approaches. As the connected segments approach requires predicted river elevations to match the observed elevations, any discrepancy between the elevation data sets can be used to provide additional information. In this case, surface uplift is inferred, which can be used to contextualise the channel steepness index values, and the processes driving variation. In this example, two signals of surface uplift are observed; the west to east increase in surface uplift in the north of the study area, and the removal of this gradient in the south. We may interpret the northern signal as westward tilting of the range, which causes greater uplift in the eastern Sierra Nevada than on the western side. This interpretation would be consistent with the findings of multiple other geomorphic studies (Wakabayashi & Sawyer, 2001; Wakabayashi, 2013; Beeson & McCoy, 2020). However, as we move south, the removal of this gradient infers another process. We suggest 825

830 that the removal of the gradient could be related to delamination in the western
Sierra Nevada (Ducea & Saleeby, 1998; Saleeby et al., 2013; Krugh & Foreshee,
2018; Ryan et al., 2020). As the delaminated crustal block sinks through the
mantle, it is replaced with buoyant asthenosphere. The buoyant asthenosphere
supports uplift of the western Sierra Nevada, countering uplift in the east caused
835 by tilting. This removes the gradient of surface uplift in the southern part of the
study area, resulting in the relatively uniform values of surface uplift observed
in the south of the range.

5. Discussion

To explore how the approaches in this review differ, we have framed the
840 discussion around a series of questions. These questions are designed to high-
light the limitations, advantages and disadvantage of the tested approaches.
The questions, and their answers are summarised in table, and a discussion is
provided below.

5.1. Question 1 - Does the approach rely on slope or elevation?

845 The first step to calculating channel steepness is to extract a river network,
and thus the elevations of each point on a river, from a topographic map or
DEM. Approaches that use slope must then take the spatial derivative of the
elevation data in order to calculate slope. Any noise present in the elevation
data is amplified during this process (Fig. 2), which can negatively affect the
850 accuracy of the analysis. Using a synthetic profile, we show that approaches
based on the slope are less accurate than χ -based approaches that work with
elevation. Furthermore, with increasing noise, smaller scale signals within a
data set become obscured. In order to have the opportunity to discern finer
scale signals, the underlying data set must contain as little noise as possible. For
855 these reasons, it is advantageous to work directly with the extracted elevation
data, by using a χ -based approach.

Discussion Question	Approach to calculating channel steepness index				
	Slope-Area Analysis	Pixel-by-pixel	Equal sized segments	Most likely segments	Damped linear inversion
Does the approach rely on slope or elevation?	✓	✓			
Are smoothing algorithms used to combat noise?		✓			
Does the approach provide independent verification of the m/n ratio?	✓		✓	✓	✓
Are tributaries incorporated in the analysis?		✓	✓	✓	✓
Are data points averaged using segments?	✓		✓	✓	
Does the approach obey the integral expression?		✓			✓
Are segments connected/can segments covary?					✓
Can the approach incorporate data from multiple basins?					✓

Figure 14: A table summarising the answers to the discussion questions. Tick marks indicate yes, blank indicates no. Squares coloured green indicate the method is advantageous with regards to the question, whereas squares in red indicate a disadvantage.

5.2. *Question 2 - Are smoothing algorithms used to combat noise?*

For approaches based on slope, noise is problematic. In order to reduce the effects of noise, smoothing algorithms can be passed over the river profile data. However, using a smoothing algorithm can also be problematic owing to the variety of ways smoothing can be performed. As demonstrated in section 4.3.2, the choice of smoothing algorithm (e.g. moving average vs toptoolbox's CRS algorithm (Schwanghart & Scherler, 2017)) can alter the maximum value of channel steepness index calculated from a data set, and the overall spread of values calculated. Invariably, this can affect how data used to infer rock uplift and erosion rates are interpreted, and there is uncertainty as to which solution is most suitable.

Using smoothing algorithms also introduces bias, as demonstrated by the residuals calculated from our synthetic example (Fig. 5). Residual values are rarely centred on 0, and depending on which side the residuals are skewed to, river profile elevations are either systematically over or under predicted. As residuals can change depending on the smoothing methodology (Fig. 9), it is difficult to account for these biases from study to study.

Smoothing elevation data along rivers also relies on the assumption that noise is spatially uncorrelated. This means that the magnitude and direction of error is unrelated to errors immediately upstream or downstream. Although autocorrelation of errors measured along river profiles has not been studied so far, it is well known that DEM errors arise from a combination of random and systematic-like components which are autocorrelated (Oksanen & Sarjakoski, 2006). Thus, autocorrelation of errors should be expected along river profiles, but this effect is difficult to distinguish from actual patterns along the river profile.

With regards to selecting an approach to calculate channel steepness index, approaches that require prior smoothing of data are disadvantageous, compared to χ -based approaches that are not as affected by noise in the raw data set.

5.3. *Question 3 - Does the approach provide independent verification of m/n ?*

For spatially uniform incision, the detachment limited stream power model predicts that the concavity index is equivalent to m/n (Whipple & Tucker, 1999; Tucker & Whipple, 2002). However, a wide range of values have been suggested
890 for m and n . Values used for the area exponent m have varied between 1/3 and 2 (Howard & Kerby, 1983; Gallen & Fernández-Blanco, 2021), and values for n range from $n < 1$ (Whipple & Tucker, 1999; Royden & Perron, 2013; Yanites, 2018), to $n = 1$, (Goren et al., 2014; Hilley et al., 2019; Steer, 2021), to $n > 1$ (Whittaker et al., 2007; DiBiase & Whipple, 2011) and even up to $n = 7$
895 (Gallen & Fernández-Blanco, 2021). Fortunately, m and n covary (Croissant & Braun, 2014), and so the ratio between the two exponents rarely falls outside of the values 0.3 and 0.7 (Willgoose et al., 1990; Snyder et al., 2000; Roe et al., 2002; Kirby & Whipple, 2012). This reduces some of the uncertainty in the k_{sn} calculation, but even within this range of values results can vary significantly
900 (Mudd et al., 2018). It is therefore beneficial to use an approach to calculate channel steepness index that also constrains m/n .

For slope-area analysis, m/n can be calculated from the gradient of the regression through the slope-area data. However, as shown in the synthetic example (section 4.2), small amounts of noise present in the slope-area data set
905 can make fitting a regression difficult. Furthermore, in using the logarithm of the slope-area data, a bias is introduced into the regression (Davis & Sampson, 1986). These issues make slope-area analysis less suitable for calculating slope-area analysis from DEM-derived data.

Fortunately, χ can be used to constrain m/n . Assuming that tributaries
910 are in steady state and that uplift is spatially uniform, points in the network with similar elevations will have similar χ values (Perron & Royden, 2013). Therefore, on a χ -plot any tributaries should be colinear with the trunk stream. This property can be exploited to determine the most likely value of m/n for a study area, with methods to do so developed by several authors (Perron & Royden, 2013; Mudd et al., 2014; Goren et al., 2014; Hergarten et al., 2016).
915 Importantly, χ -based methods for constraining the concavity index have been

shown to be superior to slope-area methods when there are transient signals propagating through the landscape or there is spatially variable rock uplift or erosion rates (Mudd et al., 2018). Because of this, it is often beneficial to use a χ -based approach.

5.4. Question 4 - Are tributaries incorporated in the analysis?

Stream networks covering large areas can be easily obtained and extracted from global DEM data sets. However, to get the best results from slope-area analysis, tributary data often has to be discarded. If tributaries are included in the slope-area analysis, distant parts of the landscape will be collapsed to the same upstream drainage area value and therefore spatial variability in channel steepness will be treated as noise. Useful information contained in the tributaries of the stream network is ignored, and resulting maps of channel steepness index have large areas that are void of any data.

The pixel-by-pixel approach can be used to calculate channel steepness for all points on a river network, including tributaries. Maps of channel steepness index created using this approach have greater spatial resolution compared to those created with slope-area analysis. Owing to the increased spatial resolution, it can be easier to detect factors that influence the spatial pattern of channel steepness, such as climate and lithology. However, the pixel by pixel approach calculates channel steepness index for each point on the river separately, and independent of other values. Additional information that could be obtained from the data set is therefore not exploited. Consider a case where multiple nodes exist on separate tributaries, in a similar area of a catchment. If one of those nodes had an anomalously high value due to noise, or an error in the DEM, there is no way to account for the anomalously high value. The anomalous node is treated separately, and the high value of channel steepness that is calculated is used in the solution.

χ based solutions do provide a way to incorporate this information however. In an ideal example, the χ -transformation collapses the tributaries and trunk stream onto a single line. When channel steepness index values are calculated

from segments, data points within those segments come from different areas on the river network. The advantage of this is that the channel steepness calculation is based on more data points, reducing the influence of noise. The
950 disadvantage however is that the ability of these methods to discern subtle spatial variations in channel steepness index is reduced. Topographic Analysis Kit (Forte & Whipple, 2019) provides a method to increase the spatial resolution using χ -based methods. Here channel steepness can be calculated by splitting the stream network into segments at every confluence, before splitting these
955 segments further using a constant length value. This ensures that points within segments come from similar areas in the catchment. The effects of anomalous values are therefore diminished as they are averaged in a segment with multiple points.

The connected segment approach, that uses a damped linear inverse scheme,
960 also incorporates data from tributaries, and so more data points contribute to the solution compared to slope-area analysis. However, one distinct advantage of the inversion scheme is the spatial weighting given to pixels in the solution. As the damping matrix requires the solution to vary smoothly in space, the effect of anomalous values is diminished, although they influence adjacent segments.
965 This prevents channel steepness index values from varying by large amounts over lengthscales that are unrealistic. As previously described, the smoothness of the solution can be changed, and chosen with aid of an L-curve (Hansen, 1992).

5.5. Question 5 - Are data points averaged using segments?

970 The advantage of using segments is that more data points contribute to the channel steepness calculation. This provides a method to counter the effects of noise, and observe broad scale variation in channel steepness index values. This is true for slope-area analysis, and the χ based segments of equal size and most likely segments approaches. However, by averaging points in a segment,
975 some of the finer scale signals present in the data set can be lost. There is a trade off between having long segments that are less affected by noise, and small

segments that can detect finer scale signals.

Averaging segments in χ -based approaches (equal sized segments, most likely segments) can be problematic due to the assumption that uplift and erosion are
980 spatially uniform. Taking an example of two spatially distal points on a river network that have similar elevations and thus χ -values. The two spatially distal points may sample different parts of the catchment, but are averaged in the same segment for the channel steepness index calculation. This implies that the two different areas of the catchment have the same values of channel steepness
985 at similar χ values, and so have experienced the same rock uplift and erosion rates. As the spatial context of the river nodes is ignored, our ability to infer spatial drivers of channel steepness index within a single river network is limited. Furthermore, as channel steepness index must be calculated separately for each river network, there is no way to account for the information present in points
990 that are close to each other, but in different networks. Because of this, the χ -based approaches that work with segments are typically limited to small study areas.

5.6. Question 6 - Does the approach obey the integral expression?

The integral expression (equation 10) describes how the elevation of a point
995 on a river can be calculated from the sum of channel steepness values of downstream nodes. For the unconnected segment approach, there are gaps or jumps between the segments that are not accounted for in the integral expression. Predicted river elevations can become systematically over or under predicted on account of these jumps, which are then propagated upstream. With each
1000 jump between a segment, error can increase and so in a river network defined by many segments, predicted elevations can have a large error associated with them. Comparatively, the connected segment approach obeys the integral expression, as there are no gaps between the segments of the discretised river network. The advantage of this is that model error is lower than the unconnected segment approach, and predicted river elevations should be similar to
1005 the observed elevations. As such, differences between predicted elevations and

observed elevations can be used to explore properties such as surface uplift (as shown in section 4.5) and palaeotopography.

5.7. Question 7 - Are segments connected/can segments covary?

1010 As the damped connected segment approach is based on the integration, and the system of equations is solved simultaneously, it is possible that segments may covary. This is because the solution is forced to stay close to the observed river elevations. If there are anomalous values in the profile, these have to be accounted for elsewhere in the solution. For example, if one segment has
1015 an anomalous value of k_{sn} , the segments either side will have lower values of channel steepness in order to keep the predicted elevations close to the observed values. In this way, error is introduced to the solution. With the segment based approaches, the segments are calculated independently of each other. An error in one segment will therefore not influence other segments.

1020 *5.8. Question 8 - Can the approach incorporate data from multiple basins?*

As mentioned previously, it is possible to calculate channel steepness index for multiple basins using any of the approaches described here. However, only the connected segment approach is informed by the spatial context of river points across multiple basins. For the χ -based equal segment and most likely
1025 segment approaches, calculating channel steepness index across multiple basins involves extracting the river network of each individual drainage basin, and fitting segments to the χ -profile. As segment fitting can only be performed on one river network at a time, there is no way to incorporate data from neighbouring
1030 signals present across drainage basin boundaries is hindered. In contrast, the damped linear inverse scheme creates a solution for all river points across the entire study area simultaneously, utilising as much spatial data as is available.

6. Conclusions

Calculating channel steepness relies on different approaches that aim to de-
1035 tect topographic signals in longitudinal river profiles in the presence of unwanted
noise in DEMs. Here, we present several examples demonstrating that the choice
of approach will affect the calculated channel steepness values, their spatial pat-
terns and eventually even interpretations. We find that χ -based approaches are
generally superior to approaches that work with values of along-river gradients,
1040 as they are less susceptible to noise contained within DEMs and their derivatives.
As might be expected, some approaches are more useful in certain contexts com-
pared to others. For instance, unconnected segment approaches are useful for
calculating accurate values of channel steepness index and pin-pointing abrupt
changes in channel steepness index. However, these approaches are not ideal
1045 for extrapolating channel steepness information and producing maps of chan-
nel steepness. Approaches based on the forward model of landscape evolution
ensure that channel steepness values are consistent with a hydrologically condi-
tioned DEM and provide the potential to address other related problems.

There is further scope to improve calculations of channel steepness index by
1050 including geological data in analyses. For instance, we might expect a sharp
contrast in channel steepness to be caused by discrete structures, such as faults
or lithological contacts. The methods described in this review do not account
for these structures in the channel steepness calculation. For methodologies
that rely on smoothing the river profile elevations, or channel steepness values
1055 (section 2.1.2 and section 4.3.2), smoothing across adjacent river nodes that
cross a fault could be reduced to gain more representative patterns of channel
steepness index. Likewise, data, such as the positions of faults, could be in-
corporated into segment fitting algorithms (section 2.2.1), so that segments are
split based on known geological disparities. Furthermore, geological boundaries
1060 could be accounted for within the damped linear inverse scheme (described in
section 4.5.2) by altering the spatial weighting matrix. Instead of using the
spatial weighting matrix, W , to ensure values vary smoothly compared across

adjacent pixels in all directions, the weighting matrix could be adjusted so that channel steepness values of adjacent pixels that are separated by, for instance,
1065 a fault are not required to vary smoothly.

We have also shown how the analysis of channel steepness index can be extended to predict surface uplift by solving an inverse problem based on the forward model. The principle behind this is that the channel steepness values can be used to predict elevations. If these elevations disagree with the observed elevations an additional component of elevation change can be resolved. However,
1070 the resulting inverse problem is ill-posed, owing to the number of non-unique solutions that describe a small elevation data set with two parameters. To improve the resolution of the model parameters of the inverse problem, the data included in the analysis could be widened beyond just topography to include
1075 lithological and climate data. Such steps could greatly increase our understanding of how and why channel steepness varies, and ultimately what controls rock uplift, erosion and topographic evolution.

7. Acknowledgments

We would like to thank Aaron Bufe and Frank Pazzaglia for insightful, detailed reviews that greatly improved the manuscript. AS is supported by the
1080 Natural Environment Research Council [grant number NE/S007229/1]. MF is supported by the Natural Environment Research Council [grant number NE/N015479/1].

References

- 1085 Adams, B. A., Whipple, K. X., Forte, A. M., Heimsath, A. M., & Hodges, K. V. (2020). Climate controls on erosion in tectonically active landscapes. *Science Advances*, 6, eaaz3166. URL: <https://advances.sciencemag.org/lookup/doi/10.1126/sciadv.aaz3166>. doi:10.1126/sciadv.aaz3166.
- Adams, B. A., Whipple, K. X., Hodges, K. V., & Heimsath, A. M. (2016).
1090 In situ development of high-elevation, low-relief landscapes via duplex de-

formation in the Eastern Himalayan hinterland, Bhutan: Landscape Response to Hinterland Duplex. *Journal of Geophysical Research: Earth Surface*, 121, 294–319. URL: <http://doi.wiley.com/10.1002/2015JF003508>. doi:10.1002/2015JF003508.

1095 Allen, G. H., Barnes, J. B., Pavelsky, T. M., & Kirby, E. (2013). Lithologic and tectonic controls on bedrock channel form at the northwest Himalayan front. *Journal of Geophysical Research: Earth Surface*, 118, 1806–1825. URL: <http://doi.wiley.com/10.1002/jgrf.20113>. doi:10.1002/jgrf.20113.

1100 Basilici, M., Ascione, A., Megna, A., Santini, S., Tavani, S., Valente, E., & Mazzoli, S. (2020). Active Deformation and Relief Evolution in the Western Lurestan Region of the Zagros Mountain Belt: New Insights From Tectonic Geomorphology Analysis and Finite Element Modeling. *Tectonics*, 39. URL: <https://onlinelibrary.wiley.com/doi/10.1029/2020TC006402>. doi:10.1029/2020TC006402.

1105 Beeson, H. W., & McCoy, S. W. (2020). Geomorphic signatures of the transient fluvial response to tilting. *Earth Surface Dynamics*, 8, 123–159. URL: <https://esurf.copernicus.org/articles/8/123/2020/>. doi:10.5194/esurf-8-123-2020.

1110 Bernard, T., Sinclair, H. D., Gailleton, B., & Fox, M. (2021). Formation of Longitudinal River Valleys and the Fixing of Drainage Divides in Response to Exhumation of Crystalline Basement. *Geophysical Research Letters*, 48. URL: <https://onlinelibrary.wiley.com/doi/10.1029/2020GL092210>. doi:10.1029/2020GL092210.

1115 Bernard, T., Sinclair, H. D., Gailleton, B., Mudd, S. M., & Ford, M. (2019). Lithological control on the post-orogenic topography and erosion history of the Pyrenees. *Earth and Planetary Science Letters*, 518, 53–66. URL: <https://linkinghub.elsevier.com/retrieve/pii/S0012821X19302389>. doi:10.1016/j.epsl.2019.04.034.

- Campforts, B., Vanacker, V., Herman, F., Vanmaercke, M., Schwanghart,
1120 W., Tenorio, G. E., Willems, P., & Govers, G. (2020). Parameteriza-
tion of river incision models requires accounting for environmental hetero-
geneity: insights from the tropical Andes. *Earth Surface Dynamics*, 8,
447–470. URL: <https://esurf.copernicus.org/articles/8/447/2020/>.
doi:10.5194/esurf-8-447-2020.
- 1125 Cannon, J., Murphy, M., & Taylor, M. (2018). Segmented
strain accumulation in the High Himalaya expressed in river
channel steepness. *Geosphere*, 14, 1131–1149. URL: [https://pubs.geoscienceworld.org/gsa/geosphere/article/14/3/1131/
529491/Segmented-strain-accumulation-in-the-High-Himalaya](https://pubs.geoscienceworld.org/gsa/geosphere/article/14/3/1131/529491/Segmented-strain-accumulation-in-the-High-Himalaya).
1130 doi:10.1130/GES01508.1.
- Cao, W., Paterson, S., Memeti, V., Mundil, R., Anderson, J., & Schmidt,
K. (2015). Tracking paleodeformation fields in the Mesozoic central Sierra
Nevada arc: Implications for intra-arc cyclic deformation and arc tem-
pos. *Lithosphere*, 7, 296–320. URL: [https://pubs.geoscienceworld.org/
1135 lithosphere/article/7/3/296-320/145749](https://pubs.geoscienceworld.org/lithosphere/article/7/3/296-320/145749). doi:10.1130/L389.1.
- Cassel, E. J., Breecker, D. O., Henry, C. D., Larson, T. E., & Stockli,
D. F. (2014). Profile of a paleo-orogen: High topography across the
present-day Basin and Range from 40 to 23 Ma. *Geology*, 42, 1007–1010.
URL: [http://pubs.geoscienceworld.org/geology/article/42/11/
1140 1007/131395/Profile-of-a-paleo-orogen-High-topography-across](http://pubs.geoscienceworld.org/geology/article/42/11/1007/131395/Profile-of-a-paleo-orogen-High-topography-across).
doi:10.1130/G35924.1.
- Cassel, E. J., Graham, S. A., Chamberlain, C. P., & Henry, C. D. (2012).
Early Cenozoic topography, morphology, and tectonics of the northern
Sierra Nevada and western Basin and Range. *Geosphere*, 8, 229–249.
1145 URL: [http://pubs.geoscienceworld.org/geosphere/article/8/2/
229/132504/Early-Cenozoic-topography-morphology-and-tectonics](http://pubs.geoscienceworld.org/geosphere/article/8/2/229/132504/Early-Cenozoic-topography-morphology-and-tectonics).
doi:10.1130/GES00671.1.

- Cecil, M. R., Saleeby, Z., Saleeby, J., & Farley, K. (2014). Pliocene–Quaternary subsidence and exhumation of the southeastern San Joaquin Basin, California, in response to mantle lithosphere removal. *Geosphere*, *10*, 129–147. URL: <http://pubs.geoscienceworld.org/geosphere/article/10/1/129/132130/PlioceneQuaternary-subsidence-and-exhumation-of>. doi:10.1130/GES00882.1.
- Chen, C.-Y., & Willett, S. D. (2016). Graphical methods of river profile analysis to unravel drainage area change, uplift and erodibility contrasts in the Central Range of Taiwan: Graphical Methods for River Profile Analysis: A Case Study of Taiwan. *Earth Surface Processes and Landforms*, *41*, 2223–2238. URL: <https://onlinelibrary.wiley.com/doi/10.1002/esp.3986>. doi:10.1002/esp.3986.
- Clark, M. K., Maheo, G., Saleeby, J., & Farley, K. A. (2005). The non-equilibrium landscape of the southern Sierra Nevada, California. *GSA Today*, *15*, 4.
- Clubb, F. J., Mudd, S. M., Hurst, M. D., & Grieve, S. W. (2020). Differences in channel and hillslope geometry record a migrating uplift wave at the Mendocino triple junction, California, USA. *Geology*, *48*, 184–188. URL: <https://pubs.geoscienceworld.org/gsa/geology/article/48/2/184/579528/Differences-in-channel-and-hillslope-geometry>. doi:10.1130/G46939.1.
- Croissant, T., & Braun, J. (2014). Constraining the stream power law: a novel approach combining a landscape evolution model and an inversion method. *Earth Surface Dynamics*, *2*, 155–166. URL: <https://esurf.copernicus.org/articles/2/155/2014/>. doi:10.5194/esurf-2-155-2014.
- Cyr, A. J., Granger, D. E., Olivetti, V., & Molin, P. (2010). Quantifying rock uplift rates using channel steepness and cosmogenic nuclide–determined erosion rates: Examples from northern and southern Italy. *Lithosphere*, *2*, 188–198. URL: <http://pubs.geoscienceworld.org/lithosphere/article/2/>

3/188/145553/Quantifying-rock-uplift-rates-using-channel. doi:10.1130/L96.1.

1180 Cyr, A. J., Granger, D. E., Olivetti, V., & Molin, P. (2014). Distinguishing between tectonic and lithologic controls on bedrock channel longitudinal profiles using cosmogenic ^{10}Be erosion rates and channel steepness index. *Geomorphology*, *209*, 27–38. URL: <https://linkinghub.elsevier.com/retrieve/pii/S0169555X13006107>. doi:10.1016/j.geomorph.2013.12.010.

1185 Davis, J. C., & Sampson, R. J. (1986). *Statistics and data analysis in geology* volume 646. New York: Wiley.

Demoulin, A., Beckers, A., & Hubert-Ferrari, A. (2015). Patterns of Quaternary uplift of the Corinth rift southern border (N Peloponnese, Greece) revealed by fluvial landscape morphometry. *Geomorphology*, *246*, 188–204. URL: <https://linkinghub.elsevier.com/retrieve/pii/S0169555X15300143>. doi:10.1016/j.geomorph.2015.05.032.

Devrani, R., Singh, V., Mudd, S. M., & Sinclair, H. D. (2015). Prediction of flash flood hazard impact from Himalayan river profiles: IMPACT OF FLASH FLOOD. *Geophysical Research Letters*, *42*, 5888–5894. URL: <http://doi.wiley.com/10.1002/2015GL063784>. doi:10.1002/2015GL063784.

1195 DiBiase, R. A., & Whipple, K. X. (2011). The influence of erosion thresholds and runoff variability on the relationships among topography, climate, and erosion rate. *Journal of Geophysical Research*, *116*, F04036. URL: <http://doi.wiley.com/10.1029/2011JF002095>. doi:10.1029/2011JF002095.

1200 DiBiase, R. A., Whipple, K. X., Heimsath, A. M., & Ouimet, W. B. (2010). Landscape form and millennial erosion rates in the San Gabriel Mountains, CA. *Earth and Planetary Science Letters*, *289*, 134–144. URL: <https://linkinghub.elsevier.com/retrieve/pii/S0012821X09006451>. doi:10.1016/j.epsl.2009.10.036.

- 1205 Du Bray, E., & Moore, J. (1985). *Geologic map of the Olancho Quadrangle, Southern Sierra Nevada, California*. Report 1734 USGS. URL: <http://pubs.er.usgs.gov/publication/mf1734>. doi:10.3133/mf1734 edition: -.
- Ducea, M., & Saleeby, J. (1998). A Case for Delamination of the Deep Batholithic Crust beneath the Sierra Nevada, California. *International Geology Review*, 40, 78–93. URL: <https://www.tandfonline.com/doi/full/10.1080/00206819809465199>. doi:10.1080/00206819809465199. 1210
- Duvall, A. R., Harbert, S. A., Upton, P., Tucker, G. E., Flowers, R. M., & Collett, C. (2020). River patterns reveal two stages of landscape evolution at an oblique convergent margin, Marlborough Fault System, New Zealand. *Earth Surface Dynamics*, 8, 177–194. URL: <https://esurf.copernicus.org/articles/8/177/2020/>. doi:10.5194/esurf-8-177-2020. 1215
- England, P., & Molnar, P. (1990). Surface uplift, uplift of rocks, and exhumation of rocks. *Geology*, 18, 1173–1177. Publisher: Geological Society of America.
- Farr, T. G., Rosen, P. A., Caro, E., Crippen, R., Duren, R., Hensley, S., Kobrick, M., Paller, M., Rodriguez, E., Roth, L., Seal, D., Shaffer, S., Shimada, J., Umland, J., Werner, M., Oskin, M., Burbank, D., & Alsdorf, D. (2007). The Shuttle Radar Topography Mission. *Reviews of Geophysics*, 45, RG2004. URL: <https://onlinelibrary.wiley.com/doi/10.1029/2005RG000183>. doi:10.1029/2005RG000183. 1220
- Ferrier, K. L., Huppert, K. L., & Perron, J. T. (2013). Climatic control of bedrock river incision. *Nature*, 496, 206–209. URL: <http://www.nature.com/articles/nature11982>. doi:10.1038/nature11982. 1225
- Figueroa, A. M., & Knott, J. R. (2010). Tectonic geomorphology of the southern Sierra Nevada Mountains (California): Evidence for uplift and basin formation. *Geomorphology*, 123, 34–45. Publisher: Elsevier.
- 1230 Fisher, P. F., & Tate, N. J. (2006). Causes and consequences of error in digital elevation models. *Progress in Physical Geography: Earth and Environ-*

- ment, 30, 467–489. URL: <http://journals.sagepub.com/doi/10.1191/0309133306pp492ra>. doi:10.1191/0309133306pp492ra.
- 1235 Flint, J. J. (1974). Stream gradient as a function of order, magnitude, and discharge. *Water Resources Research*, 10, 969–973. URL: <http://doi.wiley.com/10.1029/WR010i005p00969>. doi:10.1029/WR010i005p00969.
- 1240 Forte, A. M., & Whipple, K. X. (2019). Short communication: The Topographic Analysis Kit (TAK) for TopoToolbox. *Earth Surface Dynamics*, 7, 87–95. URL: <https://esurf.copernicus.org/articles/7/87/2019/>. doi:10.5194/esurf-7-87-2019.
- Fox, M. (2019). A linear inverse method to reconstruct paleo-topography. *Geomorphology*, 337, 151–164. URL: <https://linkinghub.elsevier.com/retrieve/pii/S0169555X19301400>. doi:10.1016/j.geomorph.2019.03.034.
- 1245 Fox, M., Bodin, T., & Shuster, D. L. (2015). Abrupt changes in the rate of Andean Plateau uplift from reversible jump Markov Chain Monte Carlo inversion of river profiles. *Geomorphology*, 238, 1–14. URL: <https://linkinghub.elsevier.com/retrieve/pii/S0169555X15001051>. doi:10.1016/j.geomorph.2015.02.022.
- 1250 Fox, M., Carter, A., & Dai, J.-G. (2020). How Continuous Are the “Relict” Landscapes of Southeastern Tibet? *Frontiers in Earth Science*, 8, 522. URL: <https://www.frontiersin.org/article/10.3389/feart.2020.587597>. doi:10.3389/feart.2020.587597.
- 1255 Frassetto, A. M., Zandt, G., Gilbert, H., Owens, T. J., & Jones, C. H. (2011). Structure of the Sierra Nevada from receiver functions and implications for lithospheric foundering. *Geosphere*, 7, 898–921. URL: <http://pubs.geoscienceworld.org/geosphere/article/7/4/898/132474/Structure-of-the-Sierra-Nevada-from-receiver>. doi:10.1130/GES00570.1.

- 1260 Gailleton, B., Mudd, S. M., Clubb, F. J., Grieve, S. W. D., & Hurst, M. D. (2021). Impact of Changing Concavity Indices on Channel Steepness and Divide Migration Metrics. *Journal of Geophysical Research: Earth Surface*, 126. URL: <https://onlinelibrary.wiley.com/doi/10.1029/2020JF006060>. doi:10.1029/2020JF006060.
- 1265 Gailleton, B., Mudd, S. M., Clubb, F. J., Peifer, D., & Hurst, M. D. (2019). A segmentation approach for the reproducible extraction and quantification of knickpoints from river long profiles. *Earth Surface Dynamics*, 7, 211–230. URL: <https://esurf.copernicus.org/articles/7/211/2019/>. doi:10.5194/esurf-7-211-2019.
- 1270 Gallen, S. F., & Fernández-Blanco, D. (2021). A New Data-Driven Bayesian Inversion of Fluvial Topography Clarifies the Tectonic History of the Corinth Rift and Reveals a Channel Steepness Threshold. *Journal of Geophysical Research: Earth Surface*, 126. URL: <https://onlinelibrary.wiley.com/doi/10.1029/2020JF005651>. doi:10.1029/2020JF005651.
- 1275 Gallen, S. F., & Wegmann, K. W. (2017). River profile response to normal fault growth and linkage: an example from the Hellenic forearc of south-central Crete, Greece. *Earth Surface Dynamics*, 5, 161–186. URL: <https://esurf.copernicus.org/articles/5/161/2017/>. doi:10.5194/esurf-5-161-2017.
- 1280 Gilbert, G. (1877). *The Geology of the Henry Mountains (Utah)*. Technical Report US Government Printing Office Washington, D.C.
- Goren, L., Fox, M., & Willett, S. D. (2014). Tectonics from fluvial topography using formal linear inversion: Theory and applications to the Inyo Mountains, California. *Journal of Geophysical Research: Earth Surface*, 119, 1651–1681. URL: <http://doi.wiley.com/10.1002/2014JF003079>. doi:10.1002/2014JF003079.
- 1285 Hack, J. T. (1957). *Studies of Longitudinal Stream Profiles in Virginia and*

Maryland. Geological Survey Professional Paper 294-B USGS United States Government Printing Office, Washington.

1290 Hack, J. T. (1973). Stream-profile analysis and stream-gradient index. *Journal of Research of the us Geological Survey*, 1, 421–429.

Hammond, W. C., Blewitt, G., & Kreemer, C. (2016). GPS Imaging of vertical land motion in California and Nevada: Implications for Sierra Nevada uplift. *Journal of Geophysical Research: Solid Earth*, 121, 7681–7703. URL: <http://doi.wiley.com/10.1002/2016JB013458>. doi:10.1002/2016JB013458.

1295 Hansen, P. C. (1992). Analysis of discrete ill-posed problems by means of the L-curve. *SIAM review*, 34, 561–580. Publisher: SIAM.

Harel, M.-A., Mudd, S., & Attal, M. (2016). Global analysis of the stream power law parameters based on worldwide ¹⁰Be denudation rates. *Geomorphology*, 268, 184–196. URL: <https://linkinghub.elsevier.com/retrieve/pii/S0169555X16303907>. doi:10.1016/j.geomorph.2016.05.035.

1300 Harkins, N., Kirby, E., Heimsath, A., Robinson, R., & Reiser, U. (2007). Transient fluvial incision in the headwaters of the Yellow River, northeastern Tibet, China. *Journal of Geophysical Research*, 112, F03S04. URL: <http://doi.wiley.com/10.1029/2006JF000570>. doi:10.1029/2006JF000570.

1305 Harries, R. M., Gailleton, B., Kirstein, L. A., Attal, M., Whittaker, A. C., & Mudd, S. M. (2021). Impact of climate on landscape form, sediment transfer and the sedimentary record. *Earth Surface Processes and Landforms*, 46, 990–1006. URL: <https://onlinelibrary.wiley.com/doi/10.1002/esp.5075>. doi:10.1002/esp.5075.

He, C., Yang, C.-J., Rao, G., Yuan, X.-P., Roda-Boluda, D. C., Cheng, Y., Yang, R., Zhang, L., & Yao, Q. (2020). Seismic assessment of the Weihe Graben, central China: Insights from geomorphological analyses and ¹⁰Be-derived catchment denudation rates. *Geomorphology*, 359, 107151. URL: <https://doi.org/10.1016/j.geomorph.2020.107151>.

1315 //linkinghub.elsevier.com/retrieve/pii/S0169555X20301239. doi:10.
1016/j.geomorph.2020.107151.

Hergarten, S., Robl, J., & Stüwe, K. (2016). Tectonic geomorphology at
small catchment sizes – extensions of the stream-power approach and the
chi method. *Earth Surface Dynamics*, 4, 1–9. URL: [https://esurf.
1320 copernicus.org/articles/4/1/2016/](https://esurf.copernicus.org/articles/4/1/2016/). doi:10.5194/esurf-4-1-2016.

Hilley, G. E., Porder, S., Aron, F., Baden, C. W., Johnstone, S. A., Liu,
F., Sare, R., Steelquist, A., & Young, H. H. (2019). Earth’s topographic
relief potentially limited by an upper bound on channel steepness. *Nature
1325 Geoscience*, 12, 828–832. URL: [http://www.nature.com/articles/
s41561-019-0442-3](http://www.nature.com/articles/s41561-019-0442-3). doi:10.1038/s41561-019-0442-3.

Hodges, K. V., Wobus, C., Ruhl, K., Schildgen, T., & Whipple, K. (2004).
Quaternary deformation, river steepening, and heavy precipitation at the
front of the Higher Himalayan ranges. *Earth and Planetary Science Let-
1330 ters*, 220, 379–389. URL: [https://linkinghub.elsevier.com/retrieve/
pii/S0012821X04000639](https://linkinghub.elsevier.com/retrieve/pii/S0012821X04000639). doi:10.1016/S0012-821X(04)00063-9.

Holmes, K., Chadwick, O., & Kyriakidis, P. (2000). Error in a USGS 30-meter
digital elevation model and its impact on terrain modeling. *Journal of Hydrol-
ogy*, 233, 154–173. URL: [https://linkinghub.elsevier.com/retrieve/
1335 pii/S0022169400002298](https://linkinghub.elsevier.com/retrieve/pii/S0022169400002298). doi:10.1016/S0022-1694(00)00229-8.

Howard, A., & Kerby, G. (1983). Channel changes in badlands. *GSA Bulletin*,
1335 94, 739–752. URL: [https://doi.org/10.1130/0016-7606\(1983\)94<739:
CCIB>2.0.CO;2](https://doi.org/10.1130/0016-7606(1983)94<739:CCIB>2.0.CO;2). doi:10.1130/0016-7606(1983)94<739:CCIB>2.0.CO;2.

Howard, A. D., Dietrich, W. E., & Seidl, M. A. (1994). Modeling flu-
vial erosion on regional to continental scales. *Journal of Geophysical Re-
1340 search: Solid Earth*, 99, 13971–13986. URL: [http://doi.wiley.com/10.
1029/94JB00744](http://doi.wiley.com/10.1029/94JB00744). doi:10.1029/94JB00744.

- Jennings, C., Gutierrez, C., Bryant, W., Saucedo, G., & Wills, C. (2010). Geologic map of California.
- Kirby, E., & Whipple, K. (2001). Quantifying differential rock-uplift rates
1345 via stream profile analysis. *Geology*, *29*, 415–418. URL: [https://doi.org/10.1130/0091-7613\(2001\)029<0415:QDRURV>2.0.CO;2](https://doi.org/10.1130/0091-7613(2001)029<0415:QDRURV>2.0.CO;2). doi:10.1130/0091-7613(2001)029<0415:QDRURV>2.0.CO;2.
- Kirby, E., & Whipple, K. X. (2012). Expression of active tectonics in erosional landscapes. *Journal of Structural Geology*, *44*, 54–75. URL: <https://linkinghub.elsevier.com/retrieve/pii/S0191814112001691>. doi:10.1016/j.jsg.2012.07.009.
1350
- Krugh, W. C., & Foreshee, B. C. (2018). Geomorphic constraints on the incision history of the lower Kern River, southern Sierra Nevada, California. *Geosphere*, *14*, 1101–1118. Publisher: Geological Society of America.
- Lague, D., & Davy, P. (2003). Constraints on the long-term colluvial erosion law by analyzing slope-area relationships at various tectonic uplift rates in the Siwaliks Hills (Nepal). *Journal of Geophysical Research: Solid Earth*, *108*. URL: <http://doi.wiley.com/10.1029/2002JB001893>. doi:10.1029/2002JB001893.
1355
- Lancaster, S. T., & Grant, G. E. (2006). Debris dams and the relief of headwater streams. *Geomorphology*, *82*, 84–97. URL: <https://linkinghub.elsevier.com/retrieve/pii/S0169555X06001267>. doi:10.1016/j.geomorph.2005.08.020.
1360
- Le, K., Lee, J., Owen, L. A., & Finkel, R. (2007). Late Quaternary slip rates along the Sierra Nevada frontal fault zone, California: Slip partitioning across the western margin of the Eastern California Shear Zone-Basin and Range Province. *Geological Society of America Bulletin*, *119*, 240–256. URL: <https://pubs.geoscienceworld.org/gsabulletin/article/119/1-2/240-256/125357>. doi:10.1130/B25960.1.
1365

- 1370 McPhillips, D., & Brandon, M. T. (2012). Topographic evolution of the Sierra Nevada measured directly by inversion of low-temperature thermochronology. *American Journal of Science*, *312*, 90–116. URL: <http://www.ajsonline.org/cgi/doi/10.2475/02.2012.02>. doi:10.2475/02.2012.02.
- Moore, J. G., & Moring, B. C. (2013). Rangewide glaciation
1375 in the Sierra Nevada, California. *Geosphere*, *9*, 1804–1818. URL: <http://pubs.geoscienceworld.org/geosphere/article/9/6/1804/132909/Rangewide-glaciation-in-the-Sierra-Nevada>. doi:10.1130/GES00891.1.
- Morisawa, M. E. (1962). Quantitative Geomorphology of Some Watersheds
1380 in the Appalachian Plateau. *Geological Society of America Bulletin*, *73*, 1025. URL: <https://pubs.geoscienceworld.org/gsabulletin/article/73/9/1025-1046/5476>. doi:10.1130/0016-7606(1962)73[1025:QGOSWI]2.0.CO;2.
- Mudd, S. M., Attal, M., Milodowski, D. T., Grieve, S. W. D., & Valters,
1385 D. A. (2014). A statistical framework to quantify spatial variation in channel gradients using the integral method of channel profile analysis. *Journal of Geophysical Research: Earth Surface*, *119*, 138–152. URL: <http://doi.wiley.com/10.1002/2013JF002981>. doi:10.1002/2013JF002981.
- Mudd, S. M., Clubb, F. J., Gailleton, B., & Hurst, M. D. (2018).
1390 How concave are river channels? *Earth Surface Dynamics*, *6*, 505–523. URL: <https://esurf.copernicus.org/articles/6/505/2018/>. doi:10.5194/esurf-6-505-2018.
- O’Callaghan, J. F., & Mark, D. M. (1984). The extraction of drainage networks from digital elevation data. *Computer Vision, Graphics, and Image Processing*, *28*, 323–344. URL: <https://linkinghub.elsevier.com/retrieve/pii/S0734189X84800110>. doi:10.1016/S0734-189X(84)80011-0.
- Oksanen, J., & Sarjakoski, T. (2006). Uncovering the statistical and spatial characteristics of fine topographic DEM error. *International Journal of Geographi-*

- cal *Information Science*, 20, 345–369. URL: <http://www.tandfonline.com/doi/abs/10.1080/13658810500433891>. doi:10.1080/13658810500433891.
- 1400
- Parker, R. L. (1994). *Geophysical Inverse Theory*. Princeton University Press. URL: <https://doi.org/10.1515/9780691206837>. doi:10.1515/9780691206837.
- Perron, J. T., & Royden, L. (2013). An integral approach to bedrock river profile analysis. *Earth Surface Processes and Landforms*, 38, 570–576. URL: <http://doi.wiley.com/10.1002/esp.3302>. doi:10.1002/esp.3302.
- 1405
- Playfair, J. (1802). *Illustrations of the Huttonian Theory of the Earth*. Cambridge: Cambridge University Press. URL: <http://ebooks.cambridge.org/ref/id/CB09780511973086>. doi:10.1017/CB09780511973086.
- 1410
- Poage, M. A., & Chamberlain, C. P. (2002). Stable isotopic evidence for a Pre-Middle Miocene rain shadow in the western Basin and Range: Implications for the paleotopography of the Sierra Nevada. *Tectonics*, 21, 16–1–16–10. URL: <http://doi.wiley.com/10.1029/2001TC001303>. doi:10.1029/2001TC001303.
- 1415
- Pritchard, D., Roberts, G. G., White, N. J., & Richardson, C. N. (2009). Uplift histories from river profiles. *Geophysical Research Letters*, 36, L24301. URL: <http://doi.wiley.com/10.1029/2009GL040928>. doi:10.1029/2009GL040928.
- 1420
- Quye-Sawyer, J., Whittaker, A., & Roberts, G. (2020). Calibrating fluvial erosion laws and quantifying river response to faulting in Sardinia, Italy. *Geomorphology*, 370, 107388. URL: <https://linkinghub.elsevier.com/retrieve/pii/S0169555X20303615>. doi:10.1016/j.geomorph.2020.107388.
- 1425
- Racano, S., Schildgen, T. F., Cosentino, D., & Miller, S. R. (2021). Temporal and Spatial Variations in Rock Uplift From River-Profile Inversions at the Central Anatolian Plateau Southern Margin. *Journal of Geophysical*

Research: Earth Surface, 126. URL: <https://onlinelibrary.wiley.com/doi/10.1029/2020JF006027>. doi:10.1029/2020JF006027.

1430 Richards, F. D., Hoggard, M. J., & White, N. J. (2016). Cenozoic epeirogeny of the Indian peninsula. *Geochemistry, Geophysics, Geosystems*, 17, 4920–4954. URL: <http://doi.wiley.com/10.1002/2016GC006545>. doi:10.1002/2016GC006545.

1435 Riebe, C. S., Sklar, L. S., Lukens, C. E., & Shuster, D. L. (2015). Climate and topography control the size and flux of sediment produced on steep mountain slopes. *Proceedings of the National Academy of Sciences*, 112, 15574–15579. URL: <http://www.pnas.org/lookup/doi/10.1073/pnas.1503567112>. doi:10.1073/pnas.1503567112.

1440 Roberts, G. G., & White, N. (2010). Estimating uplift rate histories from river profiles using African examples. *Journal of Geophysical Research*, 115, B02406. URL: <http://doi.wiley.com/10.1029/2009JB006692>. doi:10.1029/2009JB006692.

1445 Roberts, G. G., White, N. J., Martin-Brandis, G. L., & Crosby, A. G. (2012). An uplift history of the Colorado Plateau and its surroundings from inverse modeling of longitudinal river profiles. *Tectonics*, 31, n/a–n/a. URL: <http://doi.wiley.com/10.1029/2012TC003107>. doi:10.1029/2012TC003107.

1450 Roe, G. H., Montgomery, D. R., & Hallet, B. (2002). Effects of orographic precipitation variations on the concavity of steady-state river profiles. *Geology*, 30, 143–146. URL: [https://doi.org/10.1130/0091-7613\(2002\)030<0143:E00PV0>2.0.CO;2](https://doi.org/10.1130/0091-7613(2002)030<0143:E00PV0>2.0.CO;2). doi:10.1130/0091-7613(2002)030<0143:E00PV0>2.0.CO;2.

Royden, L., Clark, M., & Whipple, K. (2000). Evolution of river elevation profiles by bedrock incision: Analytical solutions for transient river profiles related to changing uplift and precipitation rates. *Eos Trans. AGU*, 81.

- Royden, L., & Perron, J. T. (2013). Solutions of the stream power equation and application to the evolution of river longitudinal profiles. *Journal of Geophysical Research: Earth Surface*, *118*, 497–518. URL: <http://doi.wiley.com/10.1002/jgrf.20031>. doi:10.1002/jgrf.20031.
- Rudge, J. F., Roberts, G. G., White, N. J., & Richardson, C. N. (2015). Uplift histories of Africa and Australia from linear inverse modeling of drainage inventories. *Journal of Geophysical Research: Earth Surface*, *120*, 894–914. URL: <https://onlinelibrary.wiley.com/doi/10.1002/2014JF003297>. doi:10.1002/2014JF003297.
- Ryan, J., Frassetto, A. M., Hurd, O., Jones, C. H., Unruh, J., Zandt, G., Gilbert, H., & Owens, T. J. (2020). Unusually deep earthquakes in the central Sierra Nevada (California, USA): Foundering ultramafic lithosphere? *Geosphere*, *16*, 357–377. URL: <https://pubs.geoscienceworld.org/gsa/geosphere/article/16/1/357/579801/Unusually-deep-earthquakes-in-the-central-Sierra>. doi:10.1130/GES02158.1.
- Safran, E. B., Bierman, P. R., Aalto, R., Dunne, T., Whipple, K. X., & Caffee, M. (2005). Erosion rates driven by channel network incision in the Bolivian Andes. *Earth Surface Processes and Landforms*, *30*, 1007–1024. URL: <https://onlinelibrary.wiley.com/doi/10.1002/esp.1259>. doi:10.1002/esp.1259.
- Saleeby, J., Saleeby, Z., & Le Pourhiet, L. (2013). Epeirogenic transients related to mantle lithosphere removal in the southern Sierra Nevada region, California: Part II. Implications of rock uplift and basin subsidence relations. *Geosphere*, *9*, 394–425. URL: <http://pubs.geoscienceworld.org/geosphere/article/9/3/394/132575/Epeirogenic-transients-related-to-mantle>. doi:10.1130/GES00816.1.
- Scherler, D., Bookhagen, B., & Strecker, M. R. (2014). Tectonic control on 10Be-derived erosion rates in the Garhwal Himalaya, India. *Journal of Geophysical*

Research: Earth Surface, 119, 83–105. URL: <http://doi.wiley.com/10.1002/2013JF002955>. doi:10.1002/2013JF002955.

1485 Schneider, H., Schwab, M., & Schlunegger, F. (2008). Channelized and hillslope sediment transport and the geomorphology of mountain belts. *International Journal of Earth Sciences*, 97, 179–192. URL: <http://link.springer.com/10.1007/s00531-006-0164-9>. doi:10.1007/s00531-006-0164-9.

Schwanghart, W., Ryan, M., & Korup, O. (2018). Topographic and Seismic
1490 Constraints on the Vulnerability of Himalayan Hydropower. *Geophysical Research Letters*, 45, 8985–8992. URL: <http://doi.wiley.com/10.1029/2018GL079173>. doi:10.1029/2018GL079173.

Schwanghart, W., & Scherler, D. (2014). Short Communication: TopoToolbox
2 – MATLAB-based software for topographic analysis and modeling in Earth
1495 surface sciences. *Earth Surface Dynamics*, 2, 1–7. URL: <https://esurf.copernicus.org/articles/2/1/2014/>. doi:10.5194/esurf-2-1-2014.

Schwanghart, W., & Scherler, D. (2017). Bumps in river profiles: uncertainty
assessment and smoothing using quantile regression techniques. *Earth Surface
Dynamics*, 5, 821–839. URL: <https://esurf.copernicus.org/articles/5/821/2017/>. doi:10.5194/esurf-5-821-2017.
1500

Schwanghart, W., & Scherler, D. (2020). Divide mobility controls knickpoint
migration on the Roan Plateau (Colorado, USA). *Geology*, 48, 698–702.
URL: <https://pubs.geoscienceworld.org/gsa/geology/article/48/7/698/583705/Divide-mobility-controls-knickpoint-migration-on>.
1505 doi:10.1130/G47054.1.

Seybold, H., Berghuijs, W. R., Prancevic, J. P., & Kirchner, J. W. (2021).
Global dominance of tectonics over climate in shaping river longitudinal
profiles. *Nature Geoscience*, . URL: <http://www.nature.com/articles/s41561-021-00720-5>. doi:10.1038/s41561-021-00720-5.

- 1510 Shortridge, A., & Messina, J. (2011). Spatial structure and landscape associations of SRTM error. *Remote Sensing of Environment*, 115, 1576–1587. URL: <https://linkinghub.elsevier.com/retrieve/pii/S0034425711000678>. doi:10.1016/j.rse.2011.02.017.
- Snyder, N. P., Whipple, K. X., Tucker, G. E., & Merritts, D. J. (2000). Landscape response to tectonic forcing: Digital elevation model analysis of stream profiles in the Mendocino triple junction region, northern California. *Geological Society of America Bulletin*, 112, 1250–1263. Publisher: Geological Society of America.
- 1520 Steer, P. (2021). *Short communication: Analytical models for 2D landscape evolution*. preprint Physical: Landscape Evolution: modelling and field studies. URL: <https://esurf.copernicus.org/preprints/esurf-2021-35/>. doi:10.5194/esurf-2021-35.
- Tucker, G. E. (2009). Natural experiments in landscape evolution. *Earth Surface Processes and Landforms*, 34, 1450–1460. URL: <https://onlinelibrary.wiley.com/doi/10.1002/esp.1833>. doi:10.1002/esp.1833.
- 1525 Tucker, G. E., & Whipple, K. X. (2002). Topographic outcomes predicted by stream erosion models: Sensitivity analysis and intermodel comparison. *Journal of Geophysical Research: Solid Earth*, 107, ETG 1–16. URL: <http://doi.wiley.com/10.1029/2001JB000162>. doi:10.1029/2001JB000162.
- 1530 Vanacker, V., von Blanckenburg, F., Govers, G., Molina, A., Campforts, B., & Kubik, P. W. (2015). Transient river response, captured by channel steepness and its concavity. *Geomorphology*, 228, 234–243. URL: <https://linkinghub.elsevier.com/retrieve/pii/S0169555X14004887>. doi:10.1016/j.geomorph.2014.09.013.
- 1535 Wahyudi, D. R., Sinclair, H. D., & Mudd, S. M. (2021). Progressive evolution of thrust fold topography in the frontal Himalaya. *Geomorphol-*

- ogy*, 384, 107717. URL: <https://linkinghub.elsevier.com/retrieve/pii/S0169555X21001252>. doi:10.1016/j.geomorph.2021.107717.
- 1540 Wakabayashi, J. (2013). Paleochannels, stream incision, erosion, topographic evolution, and alternative explanations of paleoaltimetry, Sierra Nevada, California. *Geosphere*, 9, 191–215. URL: <https://pubs.geoscienceworld.org/geosphere/article/9/2/191-215/132574>. doi:10.1130/GES00814.1.
- 1545 Wakabayashi, J., & Sawyer, T. L. (2001). Stream Incision, Tectonics, Uplift, and Evolution of Topography of the Sierra Nevada, California. *The Journal of Geology*, 109, 539–562. URL: <https://www.journals.uchicago.edu/doi/10.1086/321962>. doi:10.1086/321962.
- 1550 Wernicke, B., Clayton, R., Ducea, M., Jones, C. H., Park, S., Ruppert, S., Saleeby, J., Snow, J. K., Squires, L., Fliedner, M., Jiracek, G., Keller, R., Klemperer, S., Luetgert, J., Malin, P., Miller, K., Mooney, W., Oliver, H., & Phinney, R. (1996). Origin of High Mountains in the Continents: The Southern Sierra Nevada. *Science*, 271, 190–193. URL: <https://www.sciencemag.org/lookup/doi/10.1126/science.271.5246.190>. doi:10.1126/science.271.5246.190.
- 1555 Whipple, K. X., & Tucker, G. E. (1999). Dynamics of the stream-power river incision model: Implications for height limits of mountain ranges, landscape response timescales, and research needs. *Journal of Geophysical Research: Solid Earth*, 104, 17661–17674. URL: <http://doi.wiley.com/10.1029/1999JB900120>. doi:10.1029/1999JB900120.
- 1560 Whittaker, A. C., Attal, M., Cowie, P. A., Tucker, G. E., & Roberts, G. (2008). Decoding temporal and spatial patterns of fault uplift using transient river long profiles. *Geomorphology*, 100, 506–526. URL: <https://linkinghub.elsevier.com/retrieve/pii/S0169555X0800038X>. doi:10.1016/j.geomorph.2008.01.018.
- 1565 Whittaker, A. C., & Boulton, S. J. (2012). Tectonic and climatic controls on knickpoint retreat rates and landscape response times. *Journal of Geophysical*

Research: Earth Surface, 117, n/a–n/a. URL: <http://doi.wiley.com/10.1029/2011JF002157>. doi:10.1029/2011JF002157.

1570 Whittaker, A. C., Cowie, P. A., Attal, M., Tucker, G. E., & Roberts, G. P. (2007). Bedrock channel adjustment to tectonic forcing: Implications for predicting river incision rates. *Geology*, 35, 103. URL: <https://pubs.geoscienceworld.org/geology/article/35/2/103-106/129761>. doi:10.1130/G23106A.1.

1575 Willgoose, G., Bras, R. L., & Rodriguez-Iturbe, I. (1990). A model of river basin evolution. *Eos, Transactions American Geophysical Union*, 71, 1806. URL: <http://doi.wiley.com/10.1029/90E000349>. doi:10.1029/90E000349.

1580 Wobus, C., Whipple, K. X., Kirby, E., Snyder, N., Johnson, J., Spyropolou, K., Crosby, B., Sheehan, D., & Willett, S. (2006). Tectonics from topography: Procedures, promise, and pitfalls. *Special papers-geological society of america*, 398, 55. Publisher: Boulder, Colo.; Geological Society of America; 1999.

Wobus, C. W., Hodges, K. V., & Whipple, K. X. (2003). Has focused denudation sustained active thrusting at the Himalayan topographic front? *Geology*, 31, 861. URL: <https://pubs.geoscienceworld.org/geology/article/31/10/861-864/29139>. doi:10.1130/G19730.1.

1585 Yanites, B. J. (2018). The Dynamics of Channel Slope, Width, and Sediment in Actively Eroding Bedrock River Systems. *Journal of Geophysical Research: Earth Surface*, 123, 1504–1527. URL: <https://onlinelibrary.wiley.com/doi/abs/10.1029/2017JF004405>. doi:10.1029/2017JF004405.

1590 Yu, Y., Gao, S. S., Liu, K. H., & Zhao, D. (2020). Foundered lithospheric segments dropped into the mantle transition zone beneath southern California, USA. *Geology*, 48, 200–204. URL: <https://pubs.geoscienceworld.org/gsa/geology/article/48/2/200/579521/Foundered-lithospheric-segments-dropped-into-the>. doi:10.1130/G46889.1.